J. Fluid Mech. (2016), *vol.* 809, *pp.* 793–820. © Cambridge University Press 2016
doi:10.1017/jfm.2016.689

The influence of near-wall density and viscosity gradients on turbulence in channel flows

Ashish Patel[1,†], **Bendiks J. Boersma**[1] **and Rene Pecnik**[1,†]

[1]Process and Energy Department, Delft University of Technology, Leeghwaterstraat 39, 2628 CB Delft, The Netherlands

(Received 3 May 2016; revised 24 August 2016; accepted 18 October 2016; first published online 17 November 2016)

The influence of near-wall density and viscosity gradients on near-wall turbulence in a channel is studied by means of direct numerical simulation of the low-Mach-number approximation of the Navier–Stokes equations. Different constitutive relations for density ρ and viscosity μ as a function of temperature are used in order to mimic a wide range of fluid behaviours and to develop a generalised framework for studying turbulence modulations in variable-property flows. Instead of scaling the velocity solely based on local density, as done for the van Driest transformation, we derive an extension of the scaling that is based on gradients of the semilocal Reynolds number, defined as $Re_\tau^\star \equiv Re_\tau \sqrt{(\overline{\rho}/\overline{\rho}_w)}/(\overline{\mu}/\overline{\mu}_w)$ (the bar and subscript w denote Reynolds averaging and wall value respectively, while Re_τ is the friction Reynolds number based on wall values). This extension of the van Driest transformation is able to collapse velocity profiles for flows with near-wall property gradients as a function of the semilocal wall coordinate. However, flow quantities like mixing length, turbulence anisotropy and turbulent vorticity fluctuations do not show a universal scaling very close to the wall. This is attributed to turbulence modulations, which play a crucial role in the evolution of turbulent structures and turbulence energy transfer. We therefore investigate the characteristics of streamwise velocity streaks and quasistreamwise vortices and find that, similarly to turbulence statistics, the turbulent structures are also strongly governed by $Re_\tau^\star$ profiles and that their dependence on individual density and viscosity profiles is minor. Flows with near-wall gradients in $Re_\tau^\star$ ($\mathrm{d}Re_\tau^\star/\mathrm{d}y \neq 0$) show significant changes in inclination and tilting angles of quasistreamwise vortices. These structural changes are responsible for the observed modulation of the Reynolds stress generation mechanism and the inter-component energy transfer in flows with strong near-wall $Re_\tau^\star$ gradients.

Key words: boundary layer structure, turbulence simulation, turbulent boundary layers

1. Introduction

Turbulent fluid flows with large near-wall gradients of thermo-physical properties can occur in a wide range of engineering applications, where strong wall heat transfer plays an important role. The mean velocity and near-wall turbulent structures are greatly affected by near-wall gradients of, e.g., density ρ and viscosity μ.

† Email addresses for correspondence: a.patel@tudelft.nl, r.pecnik@tudelft.nl

However, the majority of studies on turbulent flow structures have been performed for constant-property flows.

The existence of near-wall turbulent structures has been known for several decades, and their structural features have been investigated in great detail. Although geometrically thin, the near-wall region that is formed by the viscous and buffer layers is responsible for a large fraction of the velocity drop (Jiménez & Moser 2007). This shear-dominated near-wall region accounts for a significant amount of turbulence production across the boundary layer and thus plays a crucial role in skin friction and heat transfer. The dominant structures of the near-wall region are streamwise velocity streaks and quasistreamwise vortices. Streaks (Kline *et al.* 1967) are spanwise modulation of streamwise velocity and consist of low- and high-speed streaks with a characteristic spacing of approximately 100 wall units in the spanwise direction (Smith & Metzler 1983). The quasistreamwise vortices, primarily found in the buffer layer, are slightly inclined away from the wall and tilted in spanwise directions (Jeong *et al.* 1997). Additionally, it is known that the dynamics of near-wall turbulence can be maintained autonomously by a self-sustaining process, where the streaks and the vortices continue to regenerate each other independently of the outer flow (Jiménez & Pinelli 1999). According to Hamilton, Kim & Waleffe (1995), the sustainment of near-wall turbulence involves a closed-loop mechanism whereby the generation of streaks is induced by quasistreamwise vortices that are in turn created by streak instability. An alternate description of the self-sustaining mechanism has been provided by Chernyshenko & Baig (2005), in which the physical mechanism of streak formation is related to the combined action of wall-normal motions, mean shear and viscous diffusion. While there are differences in the interpretation of the self-sustaining process, a close relation between low-speed streaks and quasistreamwise vortices is well established (Robinson 1991; Jeong *et al.* 1997; Jiménez & Pinelli 1999; Kim & Lim 2000; Schoppa & Hussain 2002) and is also supported by self-sustaining mechanisms described by Hamilton *et al.* (1995) and Chernyshenko & Baig (2005).

The near-wall coherent structures for variable-property wall turbulence have been far less explored in the past. Recently, Zonta, Marchioli & Soldati (2012) and Lee *et al.* (2013) have investigated incompressible flows with near-wall viscosity gradients and found that the turbulent structures are affected by these gradients. Further knowledge on variable-property effects on turbulent structures has been provided by experimental and numerical studies of supersonic flows with adiabatic walls (e.g. Spina & Smits 1987; Pirozzoli, Bernardini & Grasso 2008; Ringuette, Wu & Martin 2008; Elsinga *et al.* 2010; Lagha *et al.* 2011*b*), and cooled or heated walls (e.g. Coleman, Kim & Moser 1995; Lechner, Sesterhenn & Friedrich 2001; Foysi, Sarkar & Friedrich 2004; Morinishi, Tamano & Nakabayashi 2004; Duan, Beekman & Martin 2010; Lagha *et al.* 2011*a*; Shadloo, Hadjadj & Hussain 2015; Modesti & Pirozzoli 2016). Experimental studies on supersonic boundary layer structures are limited to the investigation of large-scale motions in the outer region of the flow, while numerical studies additionally allow a detailed investigation of near-wall structures. For supersonic boundary layers with adiabatic walls, the dynamics of near-wall turbulent structures is found to be similar to that of constant-property cases, and its characteristics scale well with the classical wall-based scaling (Pirozzoli *et al.* 2008; Ringuette *et al.* 2008; Lagha *et al.* 2011*a*). For cooled walls, the near-wall streaks extend in the streamwise direction (Coleman *et al.* 1995; Duan *et al.* 2010; Lagha *et al.* 2011*a*), while they shorten for heated walls (Lagha *et al.* 2011*a*). These streak modifications were quantified in terms of wall-based viscous units. The semilocal

scaling (Huang, Coleman & Bradshaw 1995), which uses the wall shear stress τ_w and local properties to define near-wall scales, has been shown to be effective to account for changes in streak length in the buffer layer (Morinishi *et al.* 2004; Patel *et al.* 2015). Even though the semilocal scaling is able to account for some of the differences seen between non-adiabatic variable- and constant-property flows, it has not been able to provide a universal scaling law. For instance, in a supersonic channel flow with cold isothermal walls, an increase in turbulence to mean time scale ratio was reported by Coleman *et al.* (1995) and a reduced pressure–strain rate resulting in an increased turbulence anisotropy was noted by Foysi *et al.* (2004). In a more recent study, Modesti & Pirozzoli (2016) performed direct numerical simulation (DNS) at different Reynolds and Mach numbers for compressible isothermal channel flows, and they noted an increase of streamwise turbulence intensity with Mach number as a dominant variable-property effect.

The van Driest transformed mean velocity $\overline{u}^{vD} = \int_0^{\overline{u}/u_\tau} \sqrt{\overline{\rho}/\overline{\rho}_w}\,\mathrm{d}(\overline{u}/u_\tau)$, when plotted as a function of $y^+ = yRe_\tau/h$, has been successful in collapsing velocity profiles of supersonic flows over adiabatic walls with velocity profiles from constant-property flows (Guarini *et al.* 2000; Maeder, Adams & Kleiser 2001; Duan, Beekman & Martin 2011; Lagha *et al.* 2011*a*; Pirozzoli & Bernardini 2011). Above, the bar denotes Reynolds averaging, the subscript w indicates wall values, u is the streamwise velocity, u_τ is the friction velocity, y is the wall-normal coordinate, Re_τ is the friction Reynolds number based on wall values, and h is the half-channel height or boundary layer thickness. The success of the density-weighted scaling can be attributed to Morkovin's hypothesis, which assumes that the characteristic time and length scales governing turbulent transport are not affected by changes in properties (Smits & Dussauge 2006). The van Driest transformed mean velocity $\overline{u}^{vD}$, when plotted as a function of y^+ for flows with strong near-wall gradients in density and viscosity, shows deviations if compared with profiles from constant-property flows. For cooled walls, shrinking of the viscous sublayer (Duan *et al.* 2010) and an outward shift of the log-law region with an increase in additive constant (Maeder 2000) have been noted. Recently, Trettel & Larsson (2016) derived a transformation that considers wall-normal density and viscosity gradients. They successfully applied their velocity transformation for supersonic channel flows with isothermally cooled walls. Modesti & Pirozzoli (2016) conducted a detailed comparison of different compressibility transformations and they concluded that the transformation introduced by Trettel & Larsson (2016) performs best for collapsing velocity profiles for several different compressible channel flows. However, an explanation that correlates the changes in mean velocity and the observed turbulence modulations is still missing.

In our recent work (Patel *et al.* 2015), we studied in detail the effect of variable density and viscosity on near-wall turbulence and on scaling of turbulence statistics. Similarly to constant-property turbulent channel flows, where turbulence statistics and the mean streamwise velocity $\overline{u}$ can be expressed as a function of wall-normal distance and friction Reynolds number Re_τ, we showed that turbulence statistics and the van Driest transformed mean streamwise velocity $\overline{u}^{vD}$ for variable-property turbulent flows can solely be expressed as a function of wall-normal distance and semilocal Reynolds number $Re^\star_\tau \equiv Re_\tau \sqrt{(\overline{\rho}/\overline{\rho}_w)}/(\overline{\mu}/\overline{\mu}_w)$. Unlike for constant-property flows, where turbulence statistics weakly depend on Re_τ, in variable-property flows the turbulence statistics show a strong dependence on $Re^\star_\tau$. For a case with $\mathrm{d}Re^\star_\tau/\mathrm{d}y < 0$ in the near-wall region (decreasing Reynolds number away from the wall), the streamwise normal Reynolds stress anisotropy increases, which can be associated with strengthening of large-scale low-speed streaks in the buffer layer. The reverse

was observed for $Re_\tau^\star$ profiles with $\mathrm{d}Re_\tau^\star/\mathrm{d}y > 0$. However, there are also a few similarities that can be observed for cases with different $Re_\tau^\star$ profiles. For example, the peak locations of the streamwise Reynolds stress are at similar semilocal wall distances ($y^\star = yRe_\tau^\star/h$), but their peak values differ. Another similarity is that the streamwise and spanwise non-dimensional lengths (based on semilocal scales) of turbulent structures are similar at $y^\star \approx 15$.

In the present work, our focus is on identifying the effects of near-wall property gradients on mean velocity scaling, near-wall turbulence statistics and turbulent structures. We use the same DNS database that was also used in our previous study (Patel *et al.* 2015) and supplement it with a few additional simulations. First, we derive a velocity scaling that extends the van Driest transformation to account for gradients in $Re_\tau^\star$ and that is able to provide a collapse of velocity profiles for turbulent flows with strong density and viscosity variations. We then characterise the modification of turbulent structures and show that, similarly to turbulence statistics, near-wall turbulent structures are also strongly governed by $Re_\tau^\star$ profiles. We investigate the physical mechanism that results in structural changes and consequently in modulated turbulence statistics, which explains the long-standing open question on how turbulence anisotropy is affected by wall heating or cooling (Lechner *et al.* 2001; Foysi *et al.* 2004; Modesti & Pirozzoli 2016). Even though the DNS have been performed by solving the low-Mach-number approximation of the Navier–Stokes equations, the conclusions are also applicable to high-speed flows. This is because in the near-wall region of a supersonic flow most of the near-wall density and temperature fluctuations are the result of solenoidal 'passive mixing' by turbulence, and density fluctuations show little correlation with pressure fluctuations (Coleman *et al.* 1995; Lechner *et al.* 2001).

2. Simulation details

Direct numerical simulations of fully developed turbulent channel flows, driven by a constant streamwise pressure gradient, are performed using the low-Mach-number approximation of the Navier–Stokes equations. In the low-Mach-number limit, the density and transport properties can be evaluated as a function of temperature only, independent of pressure fluctuations (Majda & Sethian 1985; Nemati *et al.* 2015). Different constitutive relations for density and viscosity are used. In order to achieve variations in temperature T, and consequently in density ρ and viscosity μ, the flow is uniformly heated with a volumetric heat source, while the temperature at both channel walls is kept constant. This allows a wall heat flux and ensures that the flow is in thermal equilibrium. Other transport properties like thermal conductivity κ and specific heat c_p are constant in all simulations. The Prandtl number based on wall quantities is taken to be unity.

The DNS code discretises the spatial derivatives in the wall-normal direction using a sixth-order staggered compact finite difference scheme (Lele 1992; Boersma 2011) and the derivatives in the spanwise and streamwise directions are computed using a Fourier expansion with periodic boundary conditions. The time integration is performed with a second-order Adams–Bashforth method, and a pressure correction scheme, based on the projection method (McMurtry *et al.* 1986), is used to ensure mass conservation. Additional details on the governing equations can be found in Patel *et al.* (2015).

Eight cases have been simulated, which are summarised in table 1. The simulations consist of three constant-property (CP395, CP150, CP550) and five variable-property cases ($CRe_\tau^\star$, $SRe_{\tau GL}^\star$, GL, LL, $SRe_{\tau LL}^\star$). The acronym CP refers to a constant-property

Case	ρ/ρ_w	μ/μ_w	Re_τ	$Re^\star_{\tau c}$	$N_x \times N_y \times N_z$	$L_x \times L_y \times L_z$
CP395	1	1	395	395	$240 \times 264 \times 240$	$2\pi h \times 2h \times \pi h$
C$Re^\star_\tau$	$(T/T_w)^{-1}$	$(T/T_w)^{-0.5}$	395	395	$240 \times 264 \times 240$	$2\pi h \times 2h \times \pi h$
S$Re^\star_{\tau GL}$	1	$(T/T_w)^{1.2}$	395	152	$360 \times 264 \times 360$	$5\pi h \times 2h \times 2\pi h$
GL	$(T/T_w)^{-1}$	$(T/T_w)^{0.7}$	395	142	$360 \times 264 \times 360$	$5\pi h \times 2h \times 2\pi h$
LL	1	$(T/T_w)^{-1}$	150	543	$360 \times 264 \times 360$	$3\pi h \times 2h \times 1.5\pi h$
S$Re^\star_{\tau LL}$	$(T/T_w)^{0.6}$	$(T/T_w)^{-0.75}$	150	535	$360 \times 264 \times 360$	$3\pi h \times 2h \times 1.5\pi h$
CP150	1	1	150	150	$192 \times 168 \times 168$	$5\pi h \times 2h \times 2\pi h$
CP550	1	1	550	550	$312 \times 312 \times 312$	$2\pi h \times 2h \times \pi h$

TABLE 1. Simulation parameters for all cases: CP395, constant-property case with $Re_\tau = 395$; C$Re^\star_\tau$, variable-property case with constant $Re^\star_\tau$ ($= 395$) across the channel; GL, case with gas-like property variations; S$Re^\star_{\tau GL}$, variable-property case with $Re^\star_\tau$ similar to case GL; LL, case with liquid-like property variations; S$Re^\star_{\tau LL}$, variable-property case with $Re^\star_\tau$ similar to case LL; CP150, constant-property case with $Re_\tau = 150$; CP550, constant-property case with $Re_\tau = 550$.

case; GL and LL refer to gas-like and liquid-like property variations respectively; C$Re^\star_\tau$ refers to a variable-property case with constant $Re^\star_\tau$ ($= 395$) across the whole channel; S$Re^\star_{\tau GL}$ refers to a variable-property case that has a similar $Re^\star_\tau$ distribution to case GL; and S$Re^\star_{\tau LL}$ refers to a variable-property case with an $Re^\star_\tau$ distribution similar to case LL. The second and third columns show the functional relations for ρ/ρ_w and μ/μ_w as a function of T/T_w. The next two columns report the wall-based friction Reynolds number Re_τ and the semilocal Reynolds number at the channel centre $Re^\star_{\tau c} = Re_\tau \sqrt{(\overline{\rho}_c/\overline{\rho}_w)}/(\overline{\mu}_c/\overline{\mu}_w)$ (the subscript c denotes the value at the channel centre). It should be noted that at the wall $Re^\star_{\tau w} = Re_\tau$. The last two columns show the number of mesh points N and the length of the domain L along the streamwise x, wall-normal y and spanwise z directions. The velocity components along the x, y and z directions are denoted as u, v and w respectively.

Figure 1 shows the distributions of density, viscosity and $Re^\star_\tau$ for all cases. Cases with variable density are shown as lines and cases with constant density are shown as symbols. As can be seen, we use different combinations of ρ and μ to obtain quasisimilar $Re^\star_\tau$ profiles. It should be noted that the strongest gradients in $Re^\star_\tau$ occur at the wall. The cases forming the first pair – CP395 and C$Re^\star_\tau$ (black symbols and line respectively, colour online) – have constant $Re^\star_\tau$ in the wall-normal direction ($\mathrm{d}Re^\star_\tau/\mathrm{d}y = 0$), even though for case C$Re^\star_\tau$ the density and viscosity are varying and decrease away from the wall. For the second pair – S$Re^\star_{\tau GL}$ and GL (blue symbols and line respectively, colour online) – the profile for $Re^\star_\tau$ decreases from 395 at the wall to approximately 150 at the channel centre. Later, we will denote these cases as $\mathrm{d}Re^\star_\tau/\mathrm{d}y < 0$. For the pair *LL* and S$Re^\star_{\tau LL}$ (red symbols and line respectively, colour online), $Re^\star_\tau$ increases from 150 at the wall to approximately 540 at the channel centre. These cases will be denoted as $\mathrm{d}Re^\star_\tau/\mathrm{d}y > 0$. The simulations CP150 (brown symbol, colour online) and CP550 (green symbol, colour online) are cases that bound the $Re^\star_\tau$ profiles of the variable-property cases in order to investigate and distinguish any Reynolds-number effects with respect to effects caused by property gradients. Considerable variations in properties have been obtained for all variable-property cases. However, the relative property fluctuations $\rho'_{rms}/\overline{\rho}$ and $\mu'_{rms}/\overline{\mu}$ (the prime denotes Reynolds average fluctuations, and the subscript *rms* indicates the root-mean-square value) are still less than 0.15 for all variable-property cases.

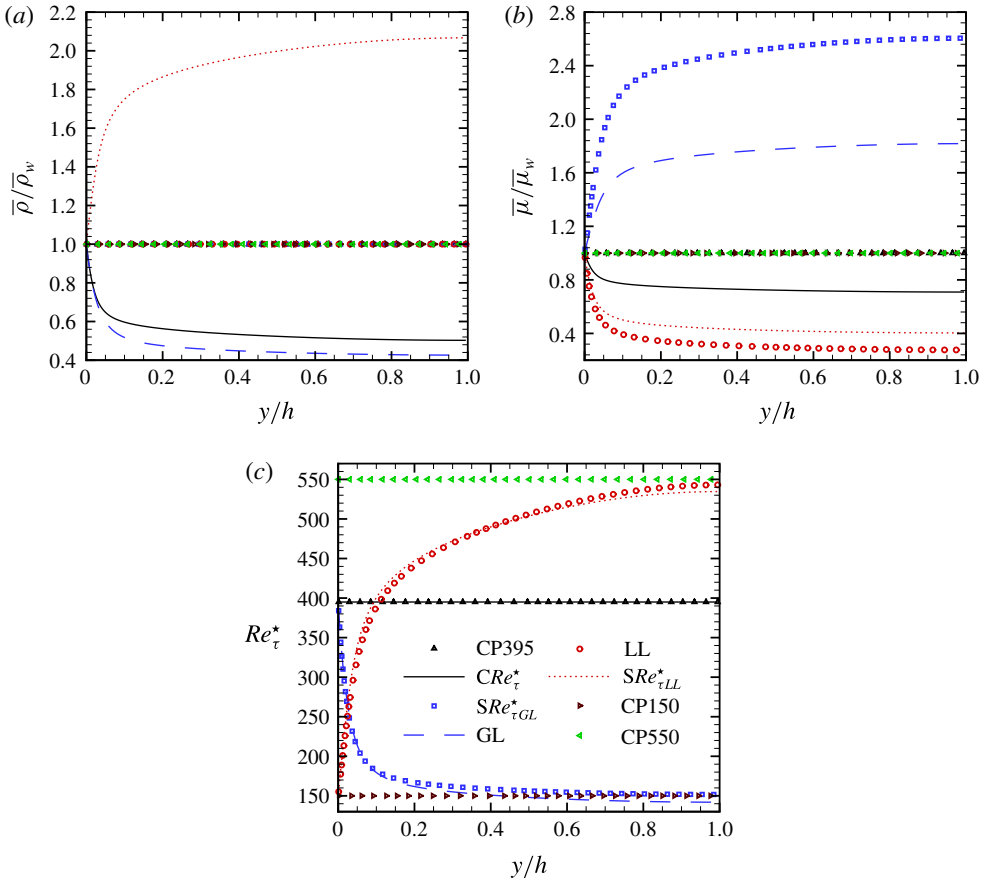

FIGURE 1. (Colour online) (*a*) Density $\overline{\rho}/\overline{\rho}_w$, (*b*) viscosity $\overline{\mu}/\overline{\mu}_w$ and (*c*) semilocal Reynolds number $Re^\star_\tau$.

The adequacy of the mesh resolution to resolve the smallest scales is evaluated by means of wall-normal distributions of Kolmogorov length scales, $\eta = ((\overline{\mu}/\overline{\rho})^3\overline{\rho}/\epsilon)^{0.25}$ (ϵ is the turbulent kinetic energy dissipation per unit volume). Figure 2 shows η, normalised by and plotted using outer scales (figure 2*a*), wall-based viscous length scales (figure 2*b*) and semilocal viscous length scales (figure 2*c*) for all cases. Cases with similar $Re^\star_\tau$ profiles show similar distributions of Kolmogorov scales, indicating that, similarly to turbulence statistics (Patel *et al.* 2015), the smallest scales are also strongly governed by $Re^\star_\tau$. The Kolmogorov scale normalised using the half-channel height increases for cases with decreasing $Re^\star_\tau$, while it decreases for cases with increasing $Re^\star_\tau$. The cases with $\mathrm{d}Re^\star_\tau/\mathrm{d}y < 0$, for which $Re^\star_\tau$ varies from 395 at the wall to approximately 140 at the channel centre, have a Kolmogorov length scale that transitions from the values of case CP395 at the wall to CP150 at the channel centre. A similar observation can be made for cases with $\mathrm{d}Re^\star_\tau/\mathrm{d}y > 0$, for which $Re^\star_\tau$ varies from 150 at the wall to approximately 540 at the centre. The Kolmogorov scale, when normalised by and plotted using classical wall-based viscous units, shows strong deviations for cases with $\mathrm{d}Re^\star_\tau/\mathrm{d}y \neq 0$. On the other hand, the use of semilocal length scales provides a good collapse of η for all cases in the near-wall region. Hence, the semilocal scaling also provides a good measure to assess the mesh

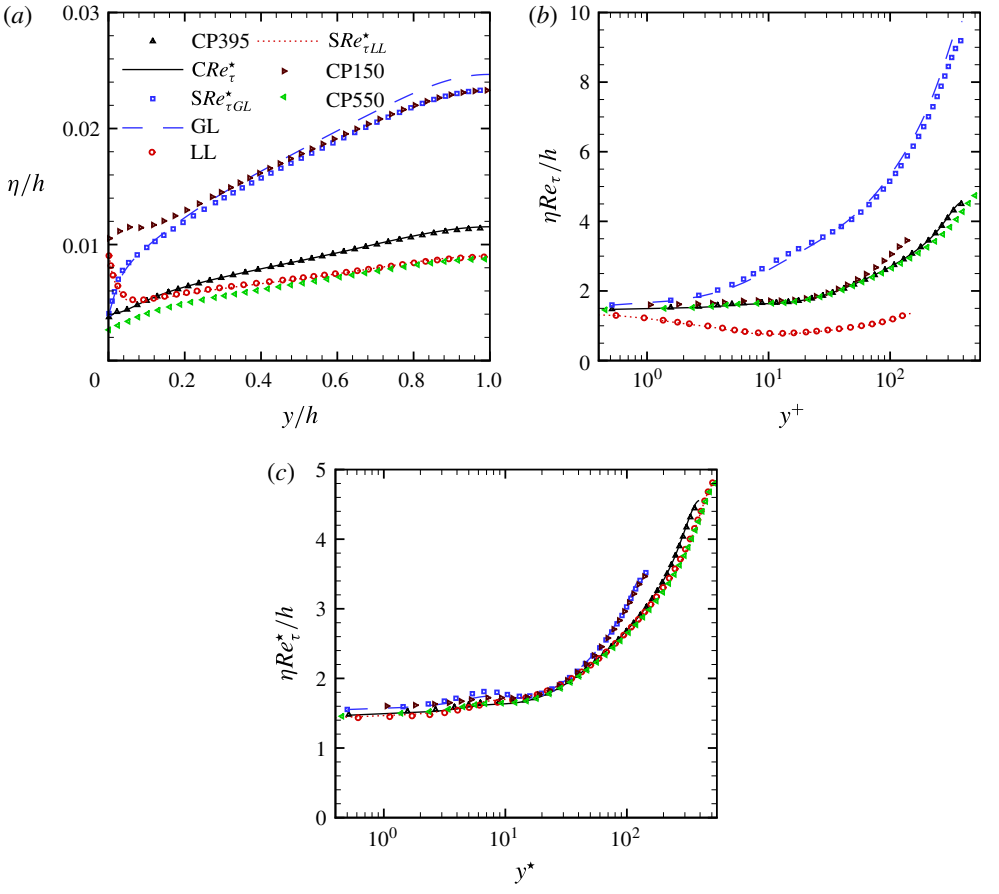

FIGURE 2. (Colour online) Kolmogorov length scale normalised by and plotted using (*a*) outer scales, (*b*) wall-based viscous length scales and (*c*) semilocal viscous length scales.

Case	$(\Delta x/\eta)_{max}$	$(\Delta(y)_{min}/\eta)_{max}$	$(\Delta(y)_{max}/\eta)_{max}$	$(\Delta z/\eta)_{max}$
CP395	6.98	0.69	0.89	3.49
$CRe^{\star}_{\tau}$	7	0.7	0.88	3.5
$SRe^{\star}_{\tau GL}$	10.78	0.64	0.43	4.31
GL	10.8	0.64	0.41	4.3
LL	5.02	0.27	1.15	2.51
$SRe^{\star}_{\tau LL}$	5.18	0.27	1.14	2.59
CP150	7.76	0.44	0.68	3.55
CP550	7.6	0.62	1	3.8

TABLE 2. Maximum spatial resolution normalised using the Kolmogorov scale η.

spacing requirements for simulations with strong fluid property variations. Table 2 lists the maximum grid spacing in terms of η for all cases, and the values are within the resolution requirements of $\Delta x < 12\eta$, $\Delta y < 2\eta$, $\Delta z < 6\eta$, as also reported in other DNS studies (Zonta *et al.* 2012; Lee *et al.* 2013).

The adequacy of the box size to accommodate the large-scale structures can be studied using the one-dimensional premultiplied energy spectrum, defined as

$$\phi_{\rho u'' u''}(k_\alpha) = k_\alpha[\mathcal{F}(\sqrt{\rho}u'')\mathcal{F}(\sqrt{\rho}u'')^*] = k_\alpha[E_{\rho u'' u''}(k_\alpha)]. \tag{2.1}$$

In the above equation, $\mathcal{F}(\psi)$ is the Fourier coefficient of ψ, $\mathcal{F}(\psi)^*$ is the complex conjugate, $E_{\rho u'' u''} = \mathcal{F}(\sqrt{\rho}u'')\mathcal{F}(\sqrt{\rho}u'')^*$ represents the energy spectrum of the density-weighted streamwise velocity fluctuation, the double prime denotes Favre-averaged fluctuations and k_α is the wavenumber in the streamwise k_x or spanwise k_z direction. The streamwise Reynolds stress is related to $\phi_{\rho u'' u''}$ and $E_{\rho u'' u''}$ as

$$\overline{\rho u'' u''} = \overline{\rho}\widetilde{u'' u''} = \int_0^\infty E_{\rho u'' u''}(k_\alpha)\,\mathrm{d}k_\alpha = \int_0^\infty \phi_{\rho u'' u''}(k_\alpha)\,\mathrm{d}(\log \lambda_\alpha), \tag{2.2}$$

where the tilde denotes Favre averaging and $\lambda_\alpha = 2\pi/k_\alpha$ is the wavelength. The area under the premultiplied spectrum, when plotted in lin-log scale, represents the Reynolds stress. A plot of $\phi_{\rho u'' u''}$, normalised by $\overline{\rho u'' u''}$ and plotted as a function of streamwise and spanwise wavelength at different wall-normal planes, is shown in figure 3. While the spanwise spectrum indicates that the spanwise box size is sufficient, it can be argued that the length of the box in the streamwise direction could be increased to resolve all of the large-scale contributions. However, as noted in previous studies (Abe, Kawamura & Choi 2004; Lozano-Durán & Jiménez 2014), the influence of these unresolved large-scale structures (due to the moderate box size) on turbulence statistics is negligible, and resolving the peak of the streamwise premultiplied spectrum (e.g. DNS data of Moser, Kim & Mansour (1999)) was considered sufficient for the present work. The spanwise premultiplied spectrum $\phi_{\rho u'' u''}(k_z)$ will be discussed in more detail in § 5 to highlight its scaling characteristics.

3. Mean velocity scaling

This section discusses the effect of near-wall gradients in density and viscosity on the scaling of mean velocity profiles. We first highlight shortcomings of the van Driest transformation for cases with strong near-wall gradients in $Re_\tau^\star$. We then derive a semilocally scaled stress-balance equation and show that the viscous stresses for the investigated cases perfectly collapse, if they are plotted as a function of the semilocal wall distance $y^\star$. We will utilise this collapse to derive a velocity scaling that will be applied for the turbulent channel flows discussed above, and for adiabatic supersonic turbulent boundary layers.

The van Driest transformed velocity $\overline{u}^{vD}$ and the diagnostic function $y\,\mathrm{d}\overline{u}^{vD}/\mathrm{d}y$ as a function of y^+ and $y^\star$ for all cases are shown in figure 4. As noted in our earlier study, cases with quasisimilar $Re_\tau^\star$ profiles (symbols and lines with the same colour online) exhibit similar $\overline{u}^{vD}$ profiles, irrespective of their individual density and viscosity profiles. However, when comparing cases with different $Re_\tau^\star$ gradients, deviations can be observed. For example, in figure 4(*a*), the slope of the linear viscous sublayer ($\overline{u}^{vD} = y^+$) increases for cases with $\mathrm{d}Re_\tau^\star/\mathrm{d}y > 0$ (red line and symbols, colour online) and decreases for cases with $\mathrm{d}Re_\tau^\star/\mathrm{d}y < 0$ (blue line and symbols, colour online). Moreover, an increase in the log-law additive constant (commonly $B = 5.2$) can be seen for cases with $\mathrm{d}Re_\tau^\star/\mathrm{d}y < 0$, while the opposite is observed for cases with $\mathrm{d}Re_\tau^\star/\mathrm{d}y > 0$. Additionally, the log-layer shifts outwards for cases with $\mathrm{d}Re_\tau^\star/\mathrm{d}y < 0$ and inwards for cases with $\mathrm{d}Re_\tau^\star/\mathrm{d}y > 0$, as can be seen from the profiles of the diagnostic function $y\,\mathrm{d}\overline{u}^{vD}/\mathrm{d}y$ in figure 4(*c*). Figure 4(*b*,*d*) shows

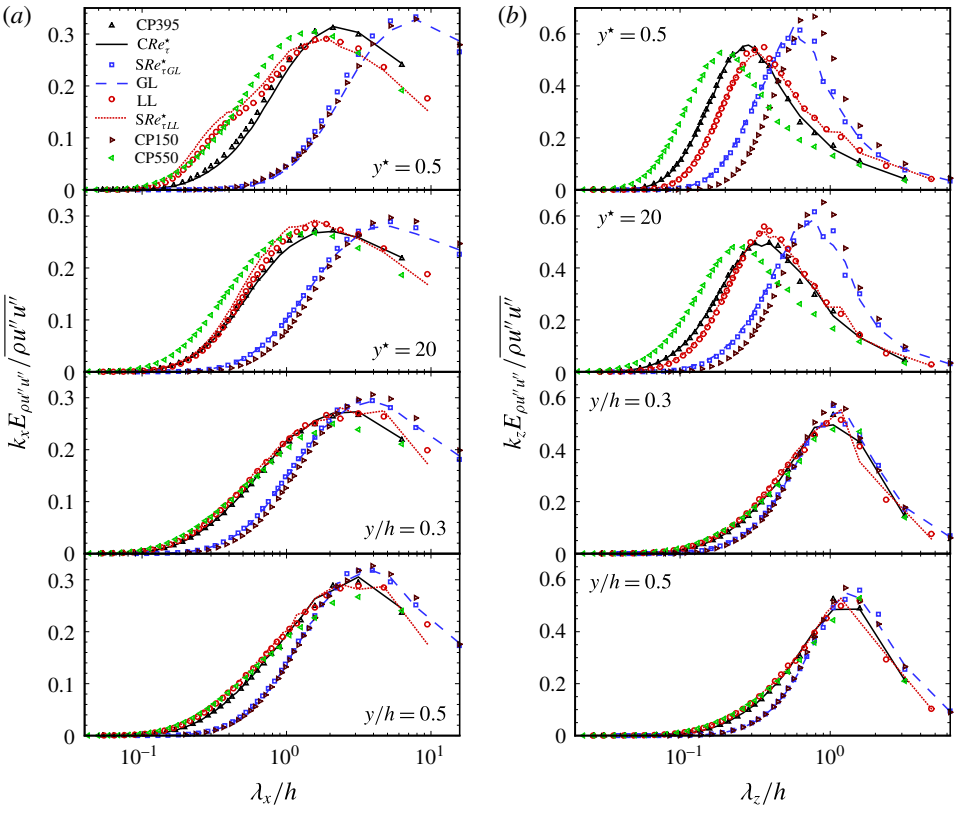

FIGURE 3. (Colour online) (*a*) Normalised premultiplied streamwise spectrum $k_x E_{\rho u'' u''}/\overline{\rho u'' u''}$ as a function of streamwise wavelength λ_x/h and (*b*) normalised premultiplied spanwise spectrum $k_z E_{\rho u'' u''}/\overline{\rho u'' u''}$ as a function of spanwise wavelength λ_z/h, at different wall-normal locations.

$\overline{u}^{vD}$ and the diagnostic function for all cases as a function of $y^{\star}$. The deviation of $\overline{u}^{vD}$ for cases with $\mathrm{d}Re^{\star}_{\tau}/\mathrm{d}y \neq 0$ is even more prominent if plotted as a function of $y^{\star}$. On the other hand, the diagnostic function collapses the onset of the log-layer if plotted as a function of $y^{\star}$. The reason for this collapse is investigated further using the streamwise stress-balance equation.

The stress-balance relation for the turbulent and viscous stresses can be obtained by integrating the mean streamwise momentum equation, which, for a fully developed turbulent channel flow (neglecting viscosity fluctuations), gives

$$-\frac{\overline{\rho}\widetilde{u''v''}}{\overline{\rho}_w u_\tau^2} + \frac{h}{Re_\tau}\left(\frac{\overline{\mu}}{\overline{\mu}_w}\right)\frac{\mathrm{d}(\overline{u}/u_\tau)}{\mathrm{d}y} \approx \frac{\tau}{\tau_w} = \left(1 - \frac{y}{h}\right), \tag{3.1}$$

where τ and τ_w are the total and wall shear stress respectively. Analogously to Patel *et al.* (2015), equation (3.1) can be written in terms of semilocally scaled velocity fluctuations (using the semilocal friction velocity $u^{\star}_{\tau} = \sqrt{\tau_w/\overline{\rho}}$)

$$\hat{u}'_i \approx \frac{u''_i}{u^{\star}_{\tau}} = \sqrt{\frac{\overline{\rho}}{\overline{\rho}_w}}\left(\frac{u''_i}{u_\tau}\right) \tag{3.2}$$

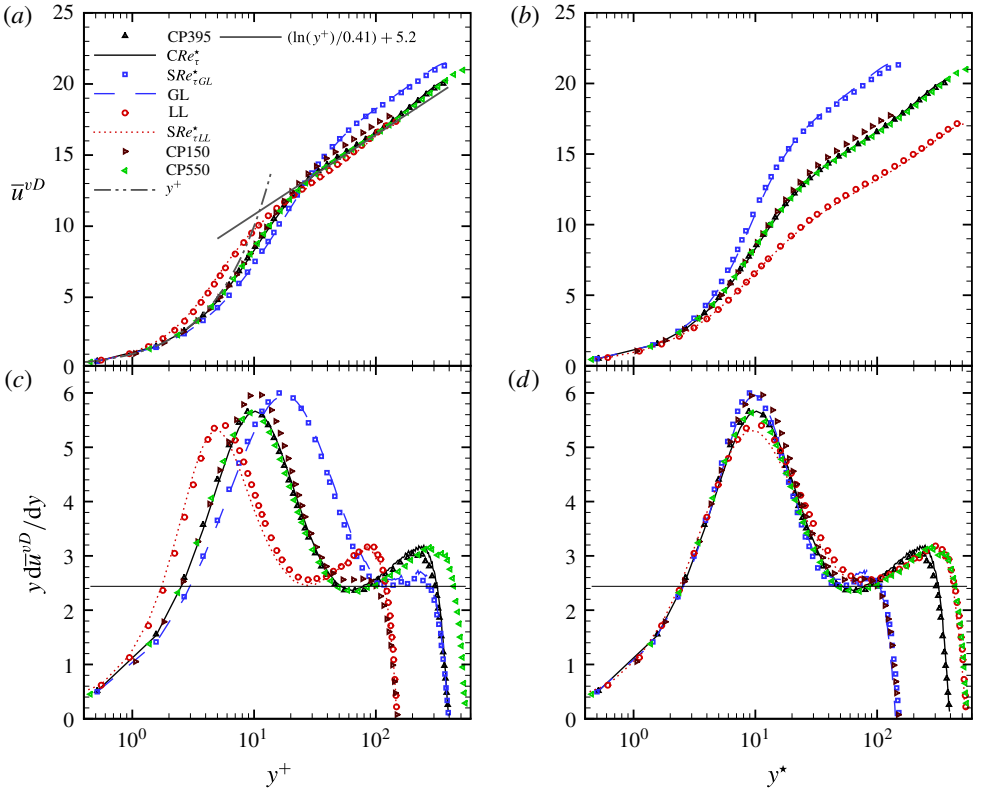

FIGURE 4. (Colour online) (*a*,*b*) van Driest velocity $\overline{u}^{vD}$ and (*c*,*d*) diagnostic function $y\,\mathrm{d}\overline{u}^{vD}/\mathrm{d}y$ shown as a function of y^+ (*a*,*c*) and $y^\star$ (*b*,*d*). The solid horizontal line in (*c*) and (*d*) has a value of $1/0.41$.

and the van Driest mean velocity increment

$$\mathrm{d}\overline{u}^{vD} = \sqrt{\frac{\overline{\rho}}{\overline{\rho}_w}}\,\mathrm{d}\left(\frac{\overline{u}}{u_\tau}\right), \tag{3.3}$$

to obtain the semilocally scaled stress-balance equation

$$-\widetilde{\hat{u}'\hat{v}'} + \frac{h}{Re^\star_\tau}\frac{\mathrm{d}\overline{u}^{vD}}{\mathrm{d}y} \approx \frac{\tau}{\tau_w} = \left(1-\frac{y}{h}\right). \tag{3.4}$$

It should be noted that the viscous stress term is a function of the van Driest mean velocity gradient, scaled by the inverse of the semilocal Reynolds number. The reason for writing (3.1) in terms of $\overline{u}^{vD}$ and $\widetilde{\hat{u}'\hat{v}'}$ originates from Patel *et al.* (2015), where the Navier–Stokes equations were rescaled using the semilocal friction velocity and local mean properties in order to obtain governing equations for the semilocally scaled mean, $\overline{u}^{vD}$, and fluctuating velocities, $\hat{u}'_i$, with $Re^\star_\tau$ as a strong parameter. In other words, the combined influence of density and viscosity variations on turbulence statistics can be characterised using a single parameter, $Re^\star_\tau$.

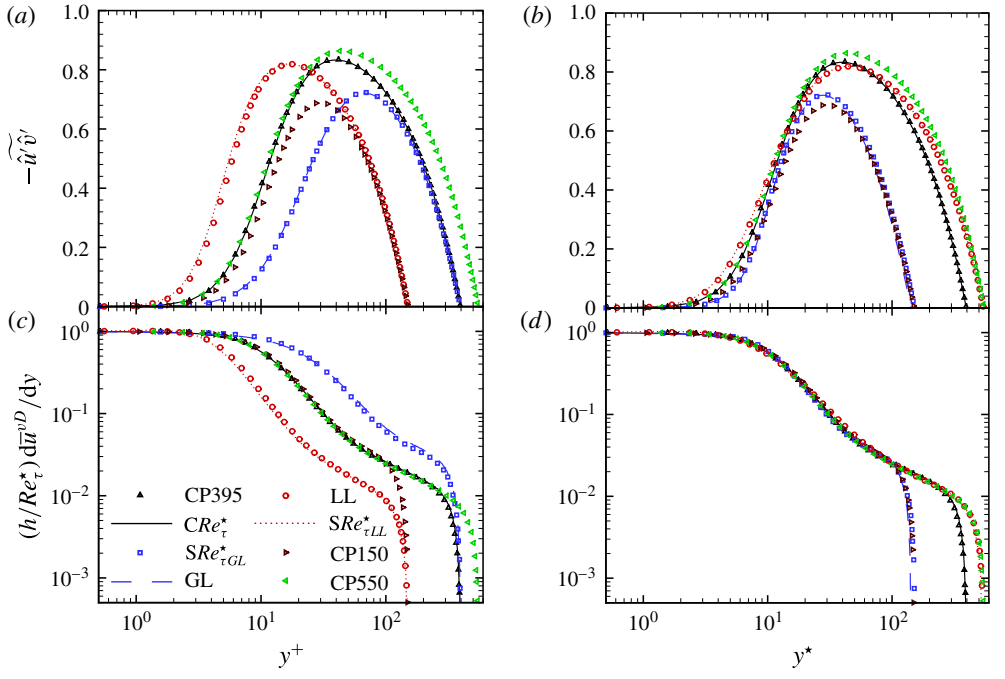

FIGURE 5. (Colour online) (*a*,*b*) Reynolds shear stress $-\widetilde{\hat{u}'\hat{v}'}$ and (*c*,*d*) viscous shear stress $(h/Re^{\star}_{\tau})\,\mathrm{d}\overline{u}^{vD}/\mathrm{d}y$ shown as a function of y^{+} (*a*,*c*) and $y^{\star}$ (*b*,*d*).

The Reynolds shear stress $\widetilde{\hat{u}'\hat{v}'}$ and viscous stress term $(h/Re^{\star}_{\tau})\,\mathrm{d}\overline{u}^{vD}/\mathrm{d}y$ in (3.4) are plotted as a function of y^{+} and $y^{\star}$ in figure 5. It is apparent that neither stress collapses if shown as a function of y^{+} (figure 5*a*,*c*) for cases with different $Re^{\star}_{\tau}$ gradients. Similar observations have been reported for compressible non-adiabatic flows in Coleman *et al.* (1995), Foysi *et al.* (2004) and Morinishi *et al.* (2004), and in Patel *et al.* (2015) for low-Mach-number channel flows with gradients in $Re^{\star}_{\tau}$. In comparison to a constant-property case with a similar Re_{τ} value, the Reynolds shear stress decreases for cases with $\mathrm{d}Re^{\star}_{\tau}/\mathrm{d}y < 0$ and increases for cases with $\mathrm{d}Re^{\star}_{\tau}/\mathrm{d}y > 0$. On the other hand, if the stresses are plotted as a function of $y^{\star}$ (figure 5*b*,*d*), two observations can be made. First, the Reynolds shear stress profiles for all cases collapse closely in the inner layer, except in the region very close to the wall where small differences can be seen. Second, and more importantly, the viscous stresses for all cases perfectly collapse over the entire $y^{\star}$ range. Given the last observation, it is evident that the viscous stress term, expressed as $(h/Re^{\star}_{\tau})\,\mathrm{d}\overline{u}^{vD}/\mathrm{d}y$, forms the basis to develop a proper scaling law for the mean velocity in flows with large density and viscosity gradients. We thus propose that the transformation must be based on the viscous stress

$$\frac{h}{Re^{\star}_{\tau}}\frac{\mathrm{d}\overline{u}^{vD}}{\mathrm{d}y} = \Phi(y^{\star}), \tag{3.5}$$

where Φ is an unknown function of $y^{\star}$. Using the chain rule $\mathrm{d}/\mathrm{d}y = (\mathrm{d}y^{\star}/\mathrm{d}y)\,\mathrm{d}/\mathrm{d}y^{\star}$, we can write (3.5) as

$$\frac{h}{Re^{\star}_{\tau}}\left(\frac{\mathrm{d}y^{\star}}{\mathrm{d}y}\right)\frac{\mathrm{d}\overline{u}^{vD}}{\mathrm{d}y^{\star}} = \Phi(y^{\star}). \tag{3.6}$$

This allows us to replace $\mathrm{d}y^\star/\mathrm{d}y$ in (3.6) by taking the derivative of $y^\star = yRe_\tau^\star/h$ with respect to y, to obtain

$$\left(1 + \frac{y}{Re_\tau^\star}\frac{\mathrm{d}Re_\tau^\star}{\mathrm{d}y}\right)\frac{\mathrm{d}\overline{u}^{vD}}{\mathrm{d}y^\star} = \Phi(y^\star). \tag{3.7}$$

Equation (3.7) thus provides the scaling law for the mean streamwise velocity, which we will denote as $\overline{u}^\star$. Hence, $\mathrm{d}\overline{u}^\star$ and $\mathrm{d}\overline{u}^{vD}$ are related through

$$\mathrm{d}\overline{u}^\star = \left(1 + \frac{y}{Re_\tau^\star}\frac{\mathrm{d}Re_\tau^\star}{\mathrm{d}y}\right)\mathrm{d}\overline{u}^{vD} = \Phi(y^\star)\,\mathrm{d}y^\star. \tag{3.8}$$

It should be noted that the transformation proposed by Trettel & Larsson (2016) is equivalent when substituting the definitions of $Re_\tau^\star$ and $d\overline{u}^{vD}$ into (3.8). Their transformation, which is expressed in terms of density and viscosity gradients, was obtained by equating the transformed log-law velocity gradient with the velocity gradient obtained from the stress-balance equation, assuming that the Reynolds shear stress is similar for compressible and constant-property cases. The present derivation follows an alternative route. It is based on rescaling the Navier–Stokes equations using the local mean properties and semilocal friction velocity, which naturally suggests that the viscous terms are scaled by the semilocal Reynolds number $Re_\tau^\star$ to account for changes in viscous scales due to property variations. The transformation expressed in terms of (3.8) thus emphasises the fact that, similarly to turbulence statistics, the transformation is also governed by the $Re_\tau^\star$ profiles, rather than individual density and viscosity profiles.

The derived velocity transformation $\overline{u}^\star = \int_0^{\overline{u}^{vD}}(1 + (y/Re_\tau^\star)\mathrm{d}Re_\tau^\star/\mathrm{d}y)\,\mathrm{d}\overline{u}^{vD}$, is shown in figure 6(*a*) as a function of $y^\star$. It can be seen that $\overline{u}^\star$ is perfectly able to collapse the velocity profiles for all cases over the entire $y^\star$ range. In our previous work (Patel *et al.* 2015), we showed that similar turbulence statistics and van Driest mean velocity profiles $\overline{u}^{vD}$ are obtained for cases with similar $Re_\tau^\star$ distributions, even if their individual mean density and viscosity profiles substantially differ. Here, we derive a transformation that accounts for gradients in $Re_\tau^\star$ in order to extend the van Driest transformation.

Using the derived velocity transformation it is also possible to explain the collapse of the diagnostic function as a function of $y^\star$, as mentioned earlier. The definitions in (3.5) and (3.8) can be expressed as

$$\frac{h}{Re_\tau^\star}\frac{\mathrm{d}\overline{u}^{vD}}{\mathrm{d}y} = \frac{\mathrm{d}\overline{u}^\star}{\mathrm{d}y^\star} = \Phi(y^\star). \tag{3.9}$$

By substituting $h/Re_\tau^\star = y/y^\star$ in (3.9) we can obtain the correlation between the diagnostic function and the newly derived velocity scale $u^\star$ as

$$y\frac{\mathrm{d}\overline{u}^{vD}}{\mathrm{d}y} = y^\star\frac{\mathrm{d}\overline{u}^\star}{\mathrm{d}y^\star} = y^\star\Phi(y^\star), \tag{3.10}$$

which explains the collapse of the diagnostic function in figure 4(*d*).

The invariance of Φ as a function of $y^\star$ can be further quantified by expressing it in terms of the turbulence mixing length. Following Huang & Coleman (1994), the

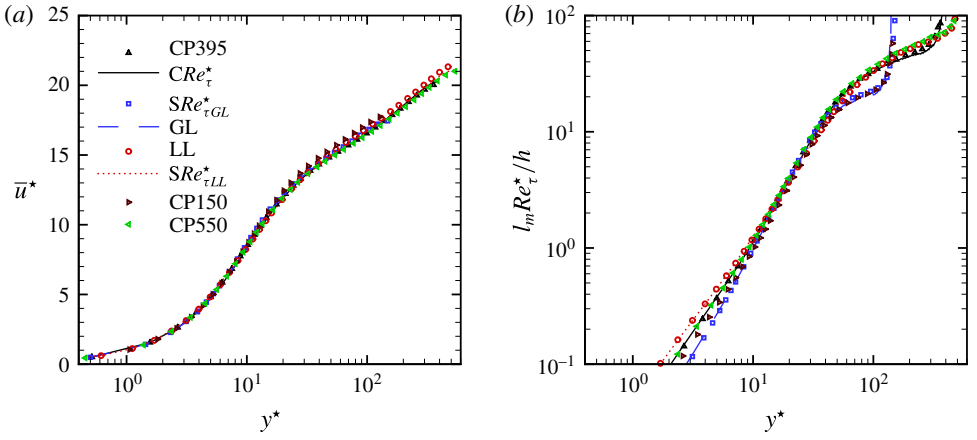

FIGURE 6. (Colour online) (*a*) Transformed velocity $\overline{u}^\star$ and (*b*) mixing length $l_m Re^\star_\tau/h$ as a function of $y^\star$.

Reynolds shear stress can be written in terms of the velocity gradient using the mixing-length theory as

$$l_m^2 = \frac{-\widetilde{u''v''}}{(\mathrm{d}\overline{u}/\mathrm{d}y)^2} = \frac{-\widetilde{\hat{u}'\hat{v}'}}{(\mathrm{d}\overline{u}^{vD}/\mathrm{d}y)^2}. \tag{3.11}$$

Substitution of the Reynolds shear stress in (3.4) using (3.11) results in a quadratic equation for $\mathrm{d}\overline{u}^{vD}/\mathrm{d}y$, which, when solved and simplified, gives

$$\Phi(y^\star) = \frac{2\tau/\tau_w}{1+\sqrt{1+4\tau/\tau_w (l_m Re^\star_\tau/h)^2}}. \tag{3.12}$$

The above expression naturally suggests that l_m scales with the semilocal length scale $h/Re^\star_\tau$. Figure 6(*b*) shows $l_m Re^\star_\tau/h$ as a function of $y^\star$. A satisfactory collapse is obtained for almost the entire inner layer, except very close to wall where small deviations occur. These deviations stem from turbulence modulation caused by strong $Re^\star_\tau$ gradients, which we will discuss in detail in §§ 4 and 5. However, close to the wall the viscous stress dominates and small values of the mixing length do not alter the velocity scaling.

In the following, we will investigate whether the scaling can also be successfully applied for supersonic adiabatic flows, for which the van Driest scaling already shows a satisfying collapse. For this we will use a DNS database for adiabatic supersonic boundary layers from Bernardini & Pirozzoli (2011) and Pirozzoli & Bernardini (2011), and data for an incompressible boundary layer from Jiménez *et al.* (2010). The investigated compressible cases have Mach numbers of $Ma = 2$, 3 and 4 and corresponding Reynolds numbers of $Re_\tau = 450$, 400 and 400 respectively. The incompressible boundary layer is at $Re_\tau = 450$. Figure 7(*a*) shows the $Re^\star_\tau$ distribution for these cases as a function of $y^\star$. It should be noted that, in contrast to the heated and cooled channel flows, the gradient of $Re^\star_\tau$ at the wall is negligible. The largest $Re^\star_\tau$ variation is obtained for the $Ma = 4$ case, where $Re^\star_\tau$ at the edge of the boundary layer is more than four times larger than at the wall. The van Driest mean velocity $\overline{u}^{vD}$ is plotted as a function of y^+ in figure 7(*b*). A satisfying collapse for the compressible and incompressible boundary layers is obtained, except in the

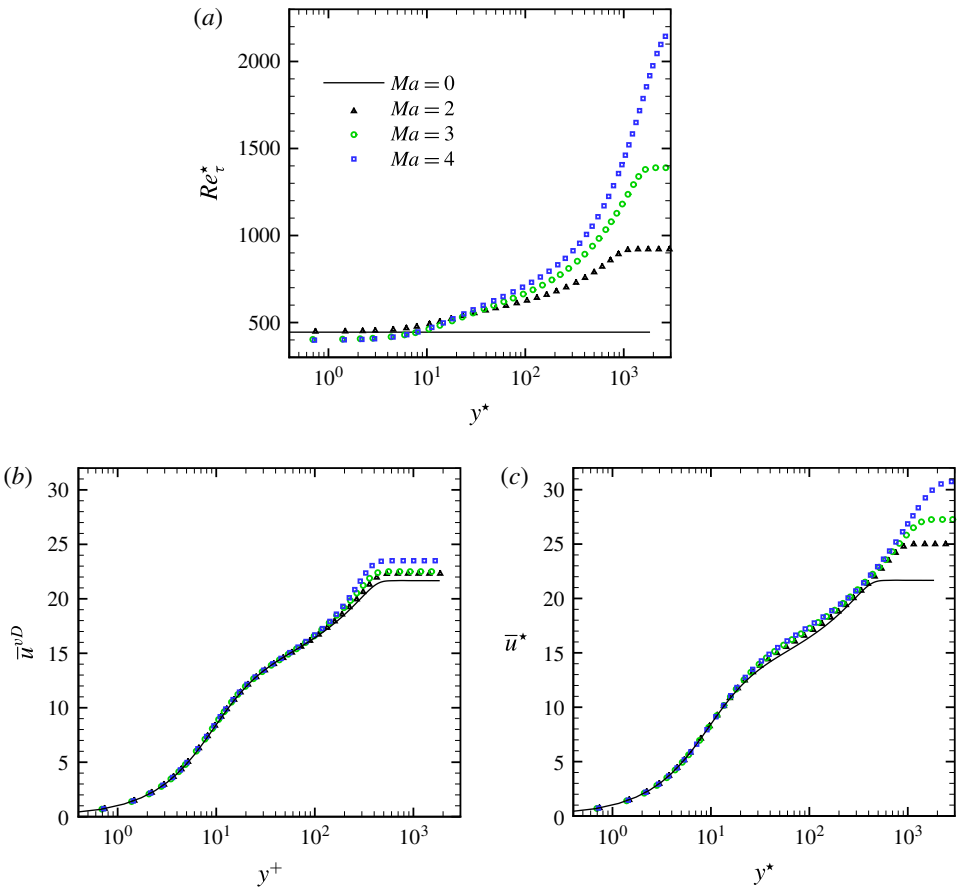

FIGURE 7. (Colour online) (*a*) The $Re_\tau^\star$ distribution shown as a function of $y^\star$, (*b*) the van Driest velocity $\overline{u}^{vD}$ shown as a function of y^+ and (*c*) the transformed velocity $\overline{u}^\star$ shown as a function of $y^\star$ for adiabatic supersonic boundary layers obtained from Bernardini & Pirozzoli (2011) and Pirozzoli & Bernardini (2011), compared with reference boundary layer data from Jiménez *et al.* (2010).

wake region, which has been studied in more detail by Zhang *et al.* (2012). The transformed velocity $\overline{u}^\star$ as a function of $y^\star$ is shown in figure 7(*c*). Here also, a reasonable collapse for the $\overline{u}^\star$ velocity profiles is obtained. However, small deviations with respect to the incompressible boundary layer occur in the buffer and logarithmic regions. Interestingly, Trettel & Larsson (2016) have also found a similar disagreement for cooled turbulent boundary layers.

The implication of the above mean velocity scaling characteristics on the stress-balance relation for these turbulent boundary layers is discussed next. The Reynolds shear and viscous stresses are shown in figure 8 as a function of y^+ and $y^\star$. Both stresses show a superior collapse if they are plotted as a function of $y^\star$. Analogously to the plot of $\overline{u}^\star$ versus $y^\star$ in figure 7(*c*), the viscous stresses of the compressible cases also deviate slightly from the incompressible case, as can be seen in figure 8(*d*). On the other hand, if the stresses are plotted as a function of y^+, it can be seen that the turbulent shear stress profiles increase and the viscous stress profiles decrease with Mach number; see figure 8(*a*,*c*). This Mach number dependence of the stresses as a

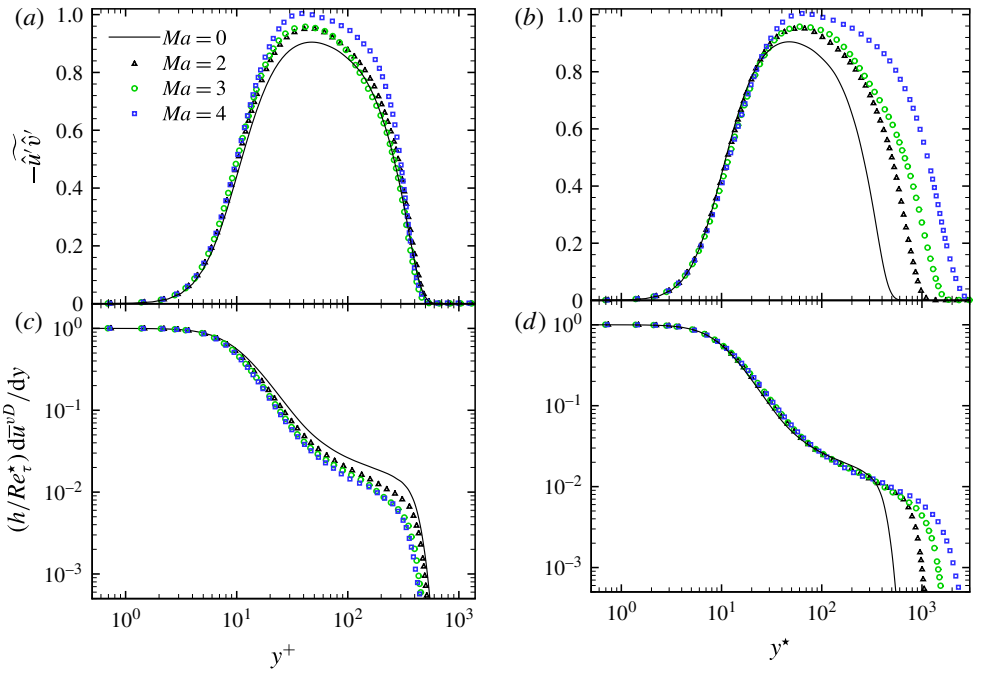

FIGURE 8. (Colour online) (*a*,*b*) Reynolds shear stress $-\widetilde{\hat{u}'\hat{v}'}$ and (*c*,*d*) viscous shear stress $(h/Re_\tau^\star)\,\mathrm{d}\overline{u}^{vD}/\mathrm{dy}$ shown as a function of y^+ (*a*,*c*) and $y^\star$ (*b*,*d*) for adiabatic supersonic boundary layers obtained from Bernardini & Pirozzoli (2011) and Pirozzoli & Bernardini (2011), compared with boundary layer data from Jiménez *et al.* (2010).

function of y^+ can be shown mathematically by writing the stress-balance equation (3.4) for the incompressible and compressible boundary layers as

$$\left(\widetilde{\hat{u}'\hat{v}'} + \frac{\tau}{\tau_w}\right)\bigg|_{incomp} = \frac{h}{Re_\tau}\frac{\mathrm{d}\overline{u}^{vD}}{\mathrm{dy}}\bigg|_{incomp} \quad \text{for the incompressible BL,} \tag{3.13}$$

$$\frac{Re_\tau^\star}{Re_\tau}\left(\widetilde{\hat{u}'\hat{v}'} + \frac{\tau}{\tau_w}\right)\bigg|_{comp} = \frac{h}{Re_\tau}\frac{\mathrm{d}\overline{u}^{vD}}{\mathrm{dy}}\bigg|_{comp} \quad \text{for the compressible BL.} \tag{3.14}$$

In the constant-stress layer, $(\tau/\tau_w)_{comp} = (\tau/\tau_w)_{incomp} = 1$, and due to the collapse of $\overline{u}^{vD}$ as a function of y^+, equations (3.13) and (3.14) can be equated as

$$(\widetilde{\hat{u}'\hat{v}'} + 1)|_{incomp} = \frac{Re_\tau^\star}{Re_\tau}(\widetilde{\hat{u}'\hat{v}'} + 1)\bigg|_{comp}. \tag{3.15}$$

Therefore, if $Re_\tau^\star > Re_\tau$, it follows that $(-\widetilde{\hat{u}'\hat{v}'})|_{comp} > (-\widetilde{\hat{u}'\hat{v}'})|_{incomp}$, which explains the Mach number dependence of the stresses. The increase in shear stress for the supersonic cases also explains the corresponding increase in turbulence intensities when compared with incompressible cases (Pirozzoli, Grasso & Gatski 2004; Bernardini & Pirozzoli 2011), due to the increase in the turbulent kinetic energy production. The partial success of both y^+ and $y^\star$ in adiabatic supersonic boundary layers thus warrants future studies. The semilocal scaling utilises the invariance of

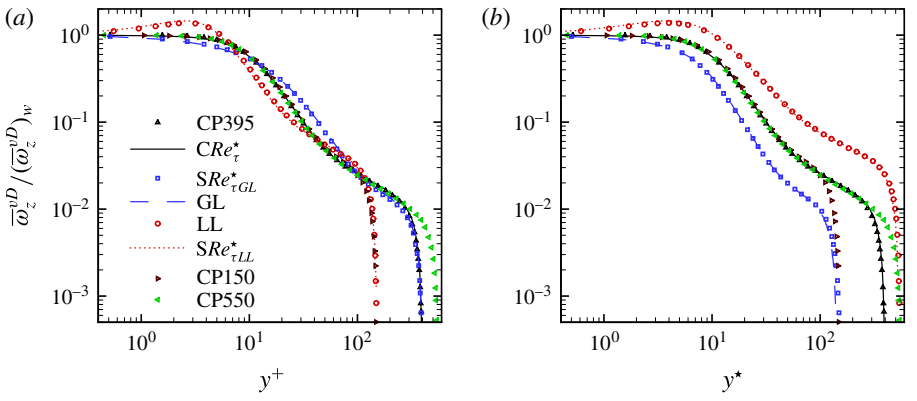

FIGURE 9. (Colour online) Wall-normalised van Driest transformed mean spanwise vorticity $\overline{\omega}_z^{vD}/(\overline{\omega}_z^{vD})_w$ shown as a function of (*a*) y^+ and (*b*) $y^\star$.

$(h/Re_\tau^\star)\mathrm{d}\overline{u}^{vD}/\mathrm{d}y$ as a function of $y^\star$ to obtain $\overline{u}^\star$, while adiabatic boundary layers exhibit invariance of a more fundamental variable, namely the wall-normalised van Driest transformed mean spanwise vorticity $\overline{\omega}_z^{vD}/(\overline{\omega}_z^{vD})_w = \mathrm{d}\overline{u}^{vD}/\mathrm{d}y^+ = (h/Re_\tau)\mathrm{d}\overline{u}^{vD}/\mathrm{d}y$, as a function of y^+. More discussion on the significance of mean vorticity is provided in the next section.

4. Influence of $Re_\tau^\star$ gradients on near-wall turbulence statistics

Turbulence statistics are strongly influenced by near-wall modifications of turbulence. Near-wall turbulence modifications for variable-property flows can be classified into two main mechanisms: (i) changes in viscous scales and (ii) structural changes of turbulence. The semilocal scaling is successful in collapsing turbulence statistics, such as mean velocity (see figure 6*a*), Reynolds and viscous shear stress (see figure 5*b*,*d*), because it accommodates the change in viscous scales using local quantities, and because these quantities are not significantly affected by structural changes and non-local effects very close to the wall. On the other hand, the semilocal scaling fails for turbulence statistics that are sensitive to strong non-local interactions of the buffer layer vortical structures with the sublayer region, e.g. statistics of vorticity fluctuations. Furthermore, the semilocal scaling also fails for turbulence statistics that contain direct information on turbulence structure, e.g. turbulence anisotropy (Foysi *et al.* 2004) and low-speed streaks (Patel *et al.* 2015).

We first study the gradient of the van Driest transformed mean velocity $\overline{u}^{vD}$, which we will refer to as the van Driest transformed mean spanwise vorticity $\overline{\omega}_z^{vD}$. The van Driest transformed mean velocity $\overline{u}^{vD}$ is the analogue to the mean velocity in a variable-density flow, and therefore a study of its gradients allows us to draw conclusions on the stability of the flow. We then discuss the turbulent vorticity fluctuations and the turbulence anisotropy to emphasise the failure of the semilocal scaling due to non-locality and changes in turbulence structure respectively.

4.1. *Mean spanwise vorticity*

The wall-normalised van Driest transformed mean spanwise vorticity $\overline{\omega}_z^{vD}/(\overline{\omega}_z^{vD})_w = \mathrm{d}\overline{u}^{vD}/\mathrm{d}y^+ = (h/Re_\tau)\mathrm{d}\overline{u}^{vD}/\mathrm{d}y$ is plotted as a function of y^+ and $y^\star$ in figures 9(*a*)

and 9(*b*) respectively. Unlike for adiabatic walls, where $\overline{\omega}_z^{vD}/(\overline{\omega}_z^{vD})_w$ is invariant as a function of y^+ in the inner layer (e.g. Pirozzoli & Bernardini 2011), $\overline{\omega}_z^{vD}/(\overline{\omega}_z^{vD})_w$ is neither a function of y^+ nor $y^\star$ for non-adiabatic walls. Based on Eyink (2008), vorticity generated at the wall is transported outward, first diffused by viscosity and subsequently advected by turbulence. Strong gradients in viscosity in the viscous-dominated region thus change the vorticity transport and consequently the mean velocity profile. The change in mean velocity profile then directly influences the turbulence. Equivalently, in variable-density flows, strong gradients in $Re_\tau^\star$ (since $Re_\tau^\star$ characterises the viscous scale) influence the van Driest transformed mean velocity profile. It is clearly visible in figure 9 that $\overline{\omega}_z^{vD}/(\overline{\omega}_z^{vD})_w$ shows a local maximum for cases with $\mathrm{d}Re_\tau^\star/\mathrm{d}y > 0$ (red line and symbols, colour online). This maximum implies an inflection point in the velocity profile, which also indicates a more unstable flow condition. The reverse happens for cases with $\mathrm{d}Re_\tau^\star/\mathrm{d}y < 0$ (blue line and symbols, colour online), where the velocity profile becomes fuller (higher negative curvature of $\mathrm{d}^2\overline{u}^{vD}/\mathrm{d}y^2$), causing the flow to become more stable (Gad-el Hak 1990). This effect is similar to flow control techniques that change the curvature of the velocity profile at the wall by introducing, e.g., wall motion, suction/injection, streamwise pressure gradients or wall-normal viscosity gradients (Gad-el Hak 1990). For example, in an adverse-pressure-gradient region (decelerated flow), the appearance of an inflection point is known to increase the wall-burst rate (Bushnell & McGinley 1989). The opposite is observed for flows with favourable pressure gradient, where the base velocity state mitigates the formation of localised near-wall inflections (Bushnell & McGinley 1989). Marquillie, Ehrenstein & Laval (2011) performed a linear stability analysis about the mean base profile of a turbulent boundary layer with adverse pressure gradient, and showed a higher streak instability for cases with a pronounced wall-normal inflection point. This fact has an important implication on near-wall turbulent structures and is discussed in more detail in § 5.

4.2. *Turbulent vorticity fluctuations*

The root-mean-squares (r.m.s.s) of the semilocally scaled turbulent vorticity fluctuations $\hat{\boldsymbol{\omega}}' = \nabla \times \hat{\boldsymbol{u}}'$ for streamwise ($\hat{\omega}_x'$), wall-normal ($\hat{\omega}_y'$) and spanwise ($\hat{\omega}_z'$) directions are shown in figure 10. Figure 10(*a*,*c*,*e*) shows the vorticity normalised by the wall-based viscous scale h/Re_τ as a function of y^+, whereas the vorticity normalised by the semilocal viscous scale $h/Re_\tau^\star$ as a function of $y^\star$ is shown in figure 10(*b*,*d*,*f*). According to our previous work (Patel *et al.* 2015), quasisimilar vorticity statistics are obtained for cases with quasisimilar $Re_\tau^\star$ profiles, even though the individual density and viscosity profiles differ. Comparison of cases with different $Re_\tau^\star$ gradients in figure 10(*a*,*c*,*e*) shows considerable differences in terms of both magnitude and wall-normal location of peak values. On the other hand, the semilocal normalisation (figure 10*b*,*d*,*f*) provides a reasonable collapse in regions away from the wall for comparable $Re_{\tau c}^\star$, and it is also able to preserve the wall-normal locations of the peaks. However, in the near-wall region the semilocal scaling with $h/Re_\tau^\star$ fails and does not provide a collapse of the vorticity profiles, even though the van Driest transformed mean spanwise vorticity scales well with $h/Re_\tau^\star$ (see figure 5*d*). In the following, we will make several comments on statistics of semilocally normalised vorticity fluctuations.

(i) It is known that even for constant-property cases the x and z vorticity fluctuation components increase with Reynolds number, whereas the y component shows Re_τ independence (Antonia & Kim 1994). This Re_τ dependence is particularly

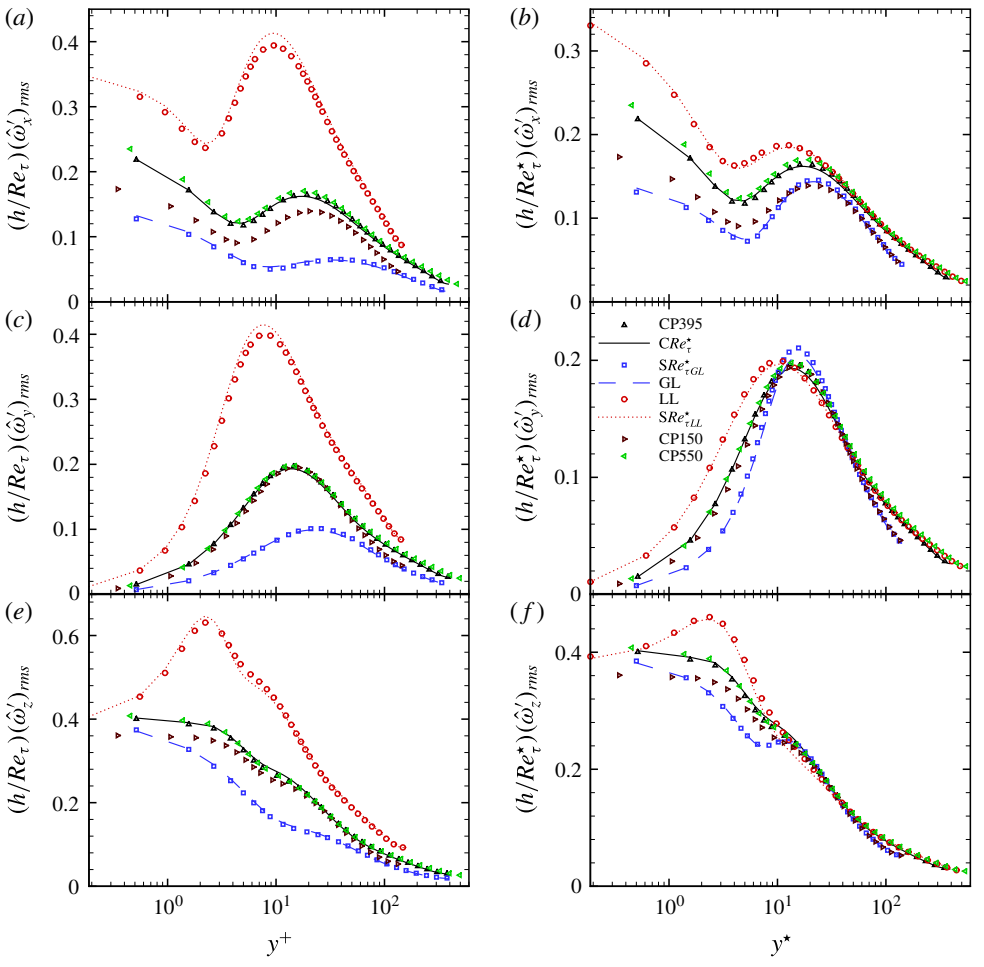

FIGURE 10. (Colour online) Root-mean-square vorticity fluctuations of (*a*,*b*) streamwise ($\hat{\omega}'_x$), (*c*,*d*) wall-normal ($\hat{\omega}'_y$) and (*e*,*f*) spanwise components ($\hat{\omega}'_z$), normalised by and plotted using wall-based scales (*a*,*c*,*e*) and semilocal scales (*b*,*d*,*f*).

prominent for the the low-Reynolds-number case CP150 (brown triangles, colour online).

(ii) For the variable-property cases, it is interesting to see that the cases with $\mathrm{d}Re^\star_\tau/\mathrm{d}y > 0$ have the highest magnitude of the semilocally scaled $\hat{\omega}'_x$ in the near-wall region, although their Re_τ values are the lowest ($Re_\tau = 150$). The opposite occurs for cases with decreasing $Re^\star_\tau$ away from the wall. There, the streamwise vorticity fluctuations are the lowest, even for comparatively high values of $Re_\tau = 395$. This is clearly a variable-property effect that is in contrast to the Reynolds number dependence as discussed in point (i). Similar observations can be made for the y and z components. The semilocally scaled r.m.s. values of $\hat{\omega}'_y$ and $\hat{\omega}'_z$ are the highest in the near-wall region for cases with $\mathrm{d}Re^\star_\tau/\mathrm{d}y > 0$, and vice versa.

(iii) For cases with $\mathrm{d}Re^\star_\tau/\mathrm{d}y > 0$, the z component has a maximum at approximately the same location where the van Driest transformed mean spanwise vorticity

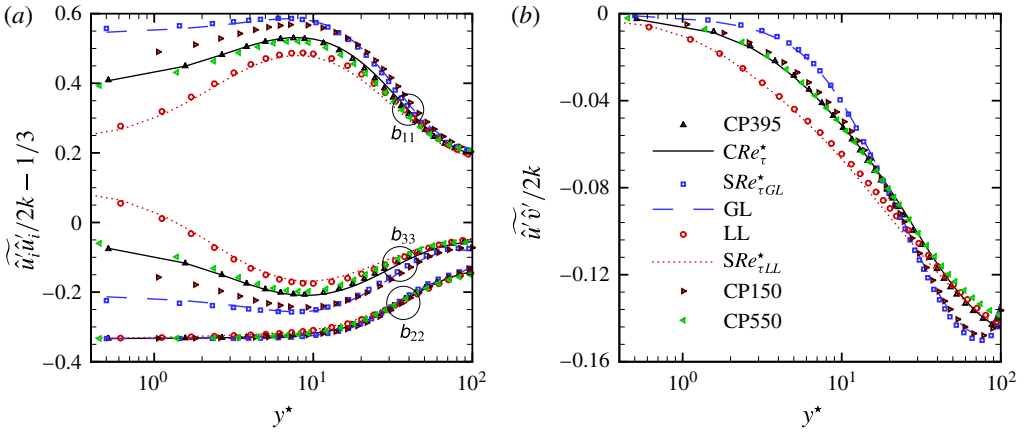

FIGURE 11. (Colour online) (*a*) Normal Reynolds stress anisotropies and (*b*) Reynolds shear stress anisotropy as a function of $y^\star$.

also shows a maximum. This is in agreement with the inflection point of the van Driest transformed mean velocity, which causes the flow to become more unstable, as mentioned in § 4.1. For cases with $\mathrm{d}Re_\tau^\star/\mathrm{d}y < 0$, the fluctuations fall off rapidly away from the wall.

The failure of the semilocal scaling is presumably caused by both structural changes in turbulence and strong non-local interactions between structures in the buffer layer and viscous sublayer which will be discussed in detail in § 5.

4.3. *Turbulent stress anisotropy*

As described earlier, and as discussed in our previous work (Patel *et al.* 2015), gradients of $Re_\tau^\star$ have a large effect on inter-component energy transfer and thus on turbulence anisotropy. The anisotropy tensor is defined as

$$b_{ij} = \frac{\widetilde{\hat{u}_i'\hat{u}_j'}}{2k} - \delta_{ij}\frac{1}{3}, \tag{4.1}$$

with the turbulent kinetic energy $k = \widetilde{\hat{u}_k'\hat{u}_k'}/2$ and δ_{ij} the Kronecker delta. Figure 11(*a*) shows that for cases with $\mathrm{d}Re_\tau^\star/\mathrm{d}y < 0$, an increase in the streamwise component b_{11} and a decrease in the spanwise component b_{33} occurs in the near-wall region if compared with cases with $\mathrm{d}Re_\tau^\star/\mathrm{d}y = 0$. The opposite is seen for cases with $\mathrm{d}Re_\tau^\star/\mathrm{d}y > 0$. The wall-normal component b_{22}, however, is not influenced by gradients in $Re_\tau^\star$. The increase in b_{11} for cases with $\mathrm{d}Re_\tau^\star/\mathrm{d}y < 0$ indicates a decrease in the redistribution of turbulent energy from the streamwise direction to the other two directions. The component b_{12}, which is the ratio of turbulent shear stress and turbulent kinetic energy, is shown in figure 11(*b*). It decreases for cases with $\mathrm{d}Re_\tau^\star/\mathrm{d}y < 0$, indicating a reduced momentum transfer in spite of higher turbulent kinetic energy, while the reverse is true for cases with $\mathrm{d}Re_\tau^\star/\mathrm{d}y > 0$. The same quantities are also shown in figure 12 for the adiabatic supersonic turbulent boundary layer cases from Bernardini & Pirozzoli (2011) and Pirozzoli & Bernardini (2011), and compared with reference boundary layer data from Jiménez *et al.* (2010).

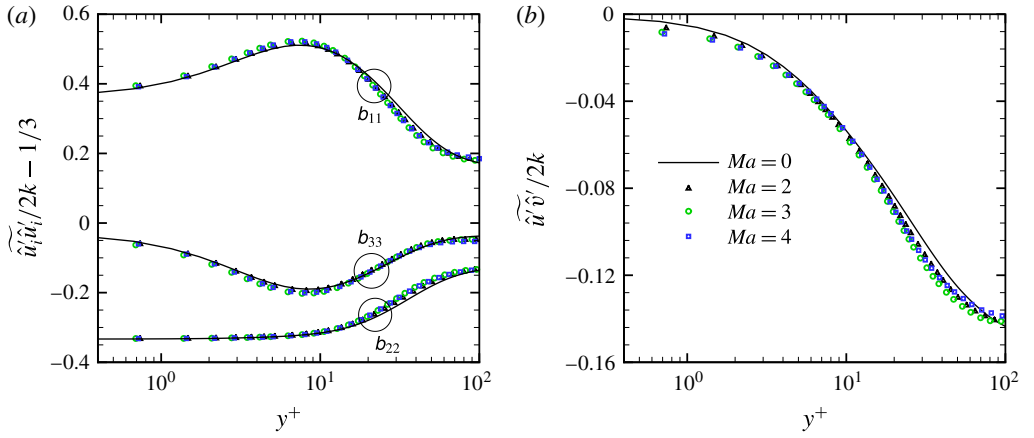

FIGURE 12. (Colour online) (*a*) Normal Reynolds stress anisotropies and (*b*) Reynolds shear stress anisotropy as a function of y^+ for adiabatic supersonic boundary layers obtained from Bernardini & Pirozzoli (2011) and Pirozzoli & Bernardini (2011), and compared with reference boundary layer data from Jiménez *et al.* (2010).

No significant changes in anisotropy are noticeable since $\mathrm{d}Re_\tau^\star/\mathrm{d}y \approx 0$ in the near-wall region. The change in anisotropy for cases with $\mathrm{d}Re_\tau^\star/\mathrm{d}y \neq 0$ is linked to modifications in turbulent structures that will be discussed next.

5. Turbulent structures

Here, we investigate the influence of near-wall $Re_\tau^\star$ gradients on the characteristics of near-wall streaks and quasistreamwise vortices, which are both known to be the dominant structures in near-wall turbulence, in order to provide a mechanistic description for the modulated statistics.

5.1. *Near-wall streaks*

For constant-property cases, the near-wall streak spacing in the viscous sublayer remains remarkably constant over a wide range of Reynolds numbers (Klewicki *et al.* 1995). Figure 13(*a*) shows the normalised premultiplied spanwise spectrum of the semilocally scaled streamwise velocity fluctuation $k_z E_{\hat{u}'\hat{u}'}/\widetilde{\hat{u}'\hat{u}'}$ at $y^\star \approx 0.5$ (top) and $y^\star \approx 13$ (bottom) as a function of the semilocally scaled wavelength $\lambda_z^\star = \lambda_z Re_\tau^\star/h$. The peak location of the spectrum represents the mean streak spacing, and it can be seen that at $y^\star \approx 13$ the spacing is the same for all cases ($\lambda_z^\star \approx 120$). This is one of the few similarities that variable-property and constant-property cases share. On the other hand, at $y^\star \approx 0.5$ only the constant-property cases (CP395, CP150, CP550) and the variable-property case C$Re_\tau^\star$ show a similar streak spacing of $\lambda_z^\star = \lambda_z^+ \approx 110$, whereas the variable-property cases with $\mathrm{d}Re_\tau^\star/\mathrm{d}y \neq 0$ show a modulation in streak spacing. The cases with $\mathrm{d}Re_\tau^\star/\mathrm{d}y < 0$ (blue lines and symbols, colour online) show an increased streak spacing of $\lambda_z^\star \approx 220$, while $\lambda_z^\star \approx 50$ for cases with $\mathrm{d}Re_\tau^\star/\mathrm{d}y > 0$ (red lines and symbols, colour online). Figure 13(*b*) gives an overview of the near-wall streak spacing as a function of $y^\star$. The lines in the plot indicate the boundaries where $k_z E_{\hat{u}'\hat{u}'}/\widetilde{\hat{u}'\hat{u}'}$ is 96 % of the peak value at a certain $y^\star$ location. It can be seen that the mean streak spacing appears to become universal after $y^\star \approx 12 - 13$, while

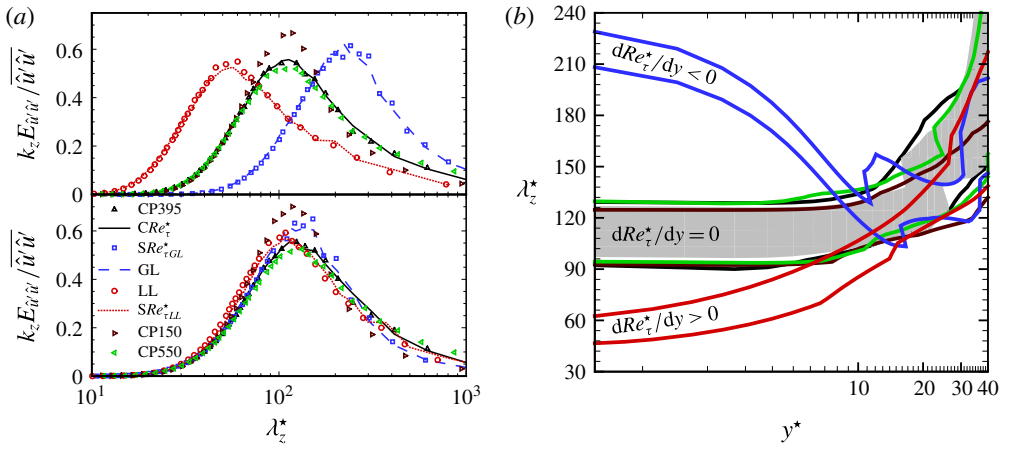

FIGURE 13. (Colour online) (*a*) Normalised premultiplied spanwise spectrum $k_z E_{\hat{u}'\hat{u}'}/\overline{\hat{u}'\hat{u}'}$ as a function of $\lambda_z^{\star}$ at $y^{\star} \approx 0.5$ (top) and $y^{\star} \approx 13$ (bottom). (*b*) Plot of $\lambda_z^{\star}$ as a function of $y^{\star}$ obtained using bands of $k_z E_{\hat{u}'\hat{u}'}/\overline{\hat{u}'\hat{u}'}$ with values larger than 96 % of its maximum value; black, brown, green, blue and red lines correspond to cases CP395, CP150, CP550, GL and LL respectively; the grey region corresponds to the case $CRe^{\star}_{\tau}$.

it deviates significantly in the viscous sublayer for cases with $d\overline{Re^{\star}_{\tau}}/dy \neq 0$. This deviation is not surprising, because of the fact that the sublayer flow is known to be induced by advecting dominant structures in the buffer layer (Kim & Hussain 1993). The wall-normal location of the dominant structures is also found to be universal in semilocal units, as shown by Pei *et al.* (2013), using a vorticity–velocity correlation in supersonic channel flows with isothermal walls at different Mach numbers. The strong non-local influence of turbulence structures in the buffer layer on the near-wall region creates a disparity between the semilocal scales and the actual turbulent scales in the sublayer.

5.2. *Vortical structures*

The three-dimensional swirling strength $\Lambda_{ci}(x, y, z)$, which is based on the imaginary part of the complex eigenvalue of the velocity gradient tensor (Zhou *et al.* 1999), is used to identify the near-wall vortical structures. The swirling strength separates swirling from shearing motion, and it can be evaluated using the gradient tensor of the instantaneous or the fluctuating velocity field. It has been analytically shown that it is not possible to decouple the mean shear from the instantaneous field (Chen *et al.* 2014). In our investigations, we evaluate the swirling strength using the instantaneous velocity gradient tensor, because the local shear depends on the instantaneous field. Similarly to Wu & Christensen (2006), we normalise the local swirling strength with its corresponding wall-normal r.m.s. $\Lambda_{ci}^{rms}(y)$ value, such that $\acute{\Lambda}_{ci}(x, y, z) = \Lambda_{ci}(x, y, z)/\Lambda_{ci}^{rms}(y)$.

Figure 14(*a*) shows the top view of an isosurface of $\acute{\Lambda}_{ci} = 1.5$ for case CP395 in the near-wall region up to $y^{+} \approx 50$. As stated in previous studies (Robinson 1991; Jeong *et al.* 1997), the near-wall region is mostly populated by quasistreamwise vortices. The isosurfaces are coloured by the sign of their streamwise vorticity, where red denotes positive and blue negative vorticity (colour online). The figure also shows a slice of

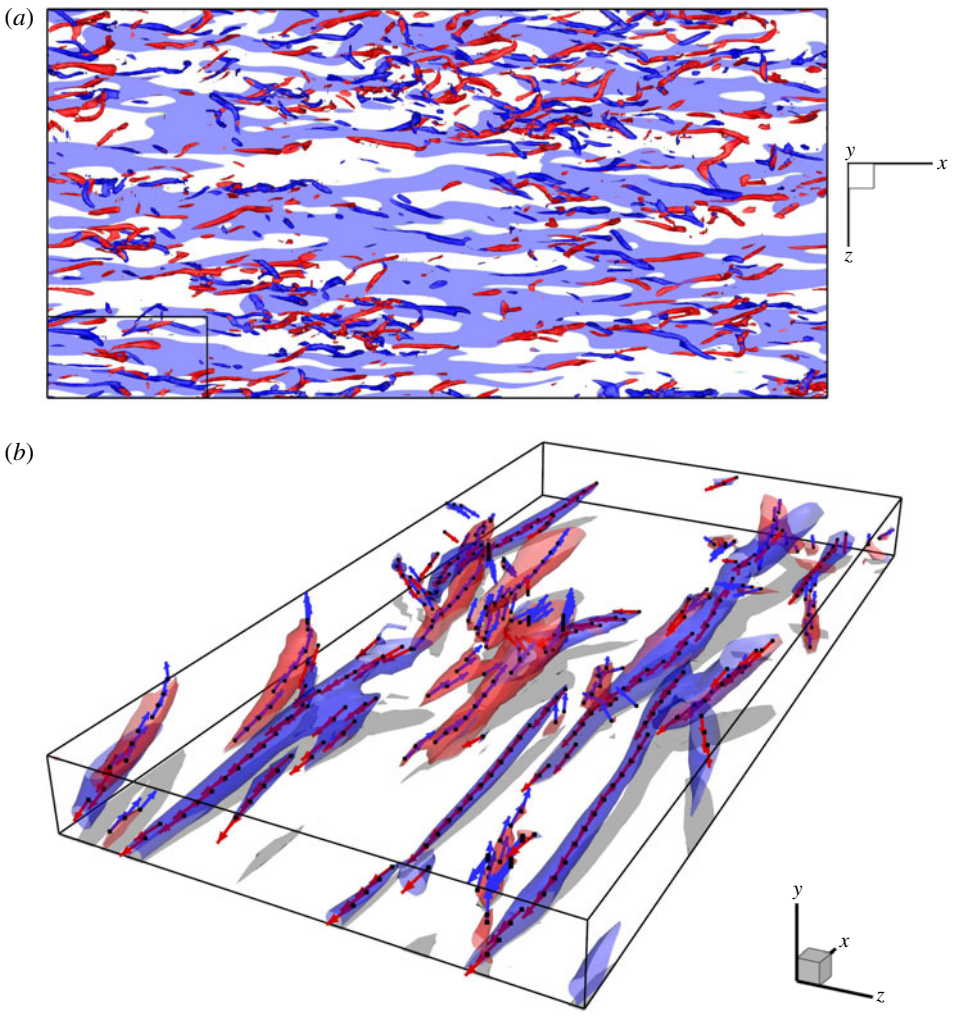

FIGURE 14. (Colour online) (*a*) Isosurfaces of swirling strength seen from the top; red isosurfaces correspond to positive vorticity while blue denotes negative vorticity; the contours show the low-speed streaks. The rectangular box corresponds to panel (*b*). (*b*) Isometric view of structures with real eigenvectors at the vortex centre; the grey colour corresponds to projection of the structures at the wall; vectors corresponding to positive vorticity are shown as blue while red denotes negative vorticity.

low-speed streaks at $y^+ = 13$ (seen as light blue online). A small section (black box) of the same instantaneous flow field is shown in an isometric view in figure 14(*b*), in order to show the inclination and elevation of these structures with respect to the wall (the grey shades are projections of the isosurfaces onto the wall). As noted by Jeong *et al.* (1997), the structures with positive vorticity tend to tilt in the negative direction and those with negative vorticity tend to tilt in the positive direction with respect to the streamwise direction within the x–z plane. This tilting is correlated with the waviness of streaks and it is associated with transfer of streamwise turbulent energy to spanwise and wall-normal components (Jeong *et al.* 1997). Therefore, study of the

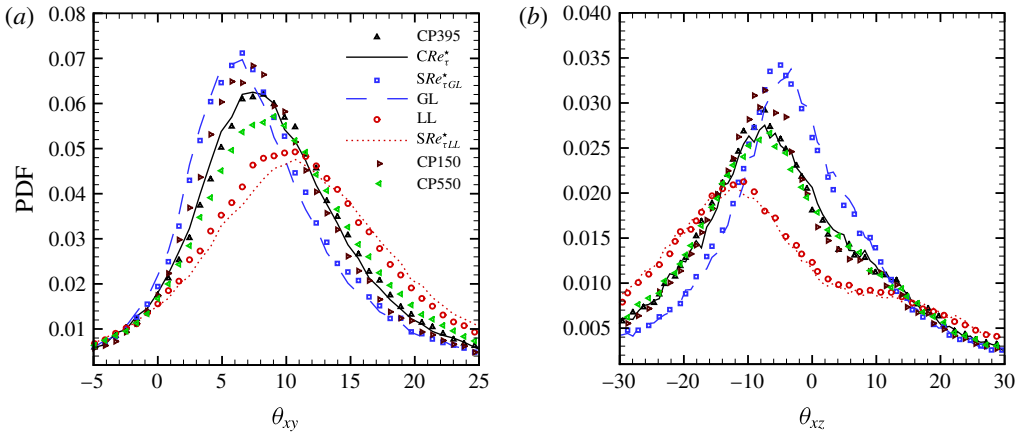

FIGURE 15. (Colour online) Probability density function of projection angle of eigenvector v_r at $y^\star = 13$: (*a*) inclination angle θ_{xy}; (*b*) tilting angle θ_{xz}.

orientation of these structures can clarify the changes in anisotropy that occur in flows with gradients in $Re^\star_\tau$.

The orientation of the vortical structures can be characterised by the real eigenvector v_r of the velocity gradient tensor, which is able to differentiate the swirling direction from the vorticity direction (Pirozzoli *et al.* 2008; Gao, Ortiz-Duenas & Longmire 2011). However, before evaluating the vortex orientation we must first find the vortex centre. This is done by performing the following steps. First, all of the grid points that correspond to the local maxima of the swirling strength Λ_{ci} are flagged in all y–z planes of the numerical domain. Next, the real eigenvector v_r of these points is used to check whether the projection angles in the perpendicular planes, which define the lift and the tilt and are denoted as θ_{xy} and θ_{xz}, are within $\pm 45°$. If this condition is met, the points are retained, otherwise they are discarded. These steps are repeated to also find the vortex centres in the z–x and x–y planes of the computational domain. Finally, only the points with $\acute{\Lambda}_{ci} \geqslant 1.5$ are kept and used as the vortex centres. It should be noted that most of vortex centres were found in the y–z plane, showing the dominance of quasistreamwise vortices. An outcome of this eduction procedure is given in figure 14(*b*), where the vortex centres with their corresponding eigenvectors are shown. Since eigenvectors can have either of the two opposing directions, the positive direction is chosen such that the dot product with the vorticity vector is positive. As is evident, the eigenvectors v_r provide an excellent measure of the orientation axis of the vortical structures. We will now apply this procedure to obtain statistics of the inclination and tilting angles to draw conclusions on turbulence modulation for all constant- and variable-property cases investigated in this work.

The probability density functions (p.d.f.s) of the inclination angle θ_{xy} and tilting angle θ_{xz} of the vortical structures at $y^\star = 13$ are shown in figure 15. Similarly to turbulence statistics, the orientation of vortical structures for cases with quasisimilar $Re^\star_\tau$ profiles also shows quasisimilarity and is therefore independent of individual density and viscosity profiles. As shown in figure 15(*a*), an increase in Re_τ from 150 to 550 for the constant-property cases increases the mode of the p.d.f. from 7° to 8° and broadens it, showing an increase in standard deviation. The variable-property cases with $\mathrm{d}Re^\star_\tau/\mathrm{d}y < 0$ (blue line and symbols, colour online) show a decrease in

the mode of the p.d.f. (6°) and a decrease in standard deviation. The opposite is seen for cases with $\mathrm{d}Re_\tau^\star/\mathrm{d}y > 0$ (red line and symbols, colour online), which show an increase in the mode (10°) and a broadening of the distribution. These results show that lifting of coherent vortical structures reduces for cases with $\mathrm{d}Re_\tau^\star/\mathrm{d}y < 0$, and increases for $\mathrm{d}Re_\tau^\star/\mathrm{d}y > 0$. This is in agreement with our previous findings (Patel *et al.* 2015), where we observed that the streaks are stabilised and do not lift as intensely for cases with $\mathrm{d}Re_\tau^\star/\mathrm{d}y < 0$, while they lift more intensely for cases with $\mathrm{d}Re_\tau^\star/\mathrm{d}y > 0$.

The tilting of the structures is indicated in figure 15(*b*). Because the direction of the tilting is coupled to the sign of the streamwise vorticity, and the events related to positive and negative streamwise vorticity are symmetric, we only show tilting angles for positive streamwise vorticity. Only small changes can be seen for the constant-property cases, with the mode at approximately ±8°. For cases with $\mathrm{d}Re_\tau^\star/\mathrm{d}y < 0$, the mode of the p.d.f.s occurs at ±5° and the distributions narrow. The reverse happens for cases with $\mathrm{d}Re_\tau^\star/\mathrm{d}y > 0$, with the mode at ±11° and broader distributions.

We will now summarise the effects related to flows with variable properties and provide a mechanistic description to explain the observed turbulence modulations. In order to avoid switching between different cases, we will only use cases with $\mathrm{d}Re_\tau^\star/\mathrm{d}y > 0$ (the effects for cases with $\mathrm{d}Re_\tau^\star/\mathrm{d}y < 0$ are exactly opposite). The increase in magnitude of the van Driest transformed mean spanwise vorticity $-\mathrm{d}\overline{u}^{vD}/\mathrm{d}y$ increases the mean forcing in the spanwise direction, causing the increased tilting of vortical structures. The increased tilting results in stronger streak waviness, which then leads to increased turbulence activity, enabling the evolution of near-wall structures and the generation of stronger shear layers (Johansson, Alfredsson & Kim 1991). The increased lifting of both streaks and vortical structures is therefore closely associated with an increase in tilting of the structures. This also explains the increase in shear stress anisotropy, which increases the momentum transfer in spite of lower turbulent kinetic energy. Furthermore, the increase in tilting angle also provides a structural interpretation for the increase in the pressure–strain correlation, which acts as a sink in the budget of the streamwise energy equation and therefore redistributes the streamwise turbulent energy in the other two directions. From Jeong *et al.* (1997), it is known that the preferential alignment of structures with respect to streamwise vorticity produces positive values of $\partial u'/\partial x$ within the structure, and since p' is negative within the structure, $p'\partial u'/\partial x$ is also negative. Additionally, the spanwise asymmetry results in internal shear layers, where high-speed fluid collides with low-speed fluid, causing a positive p' and a negative $\partial u'/\partial x$, and hence $p'\partial u'/\partial x < 0$. The modulation in tilting of the structures therefore provides a physical interpretation of the modulated turbulence statistics.

6. Conclusion

The effects of strong near-wall gradients in density and viscosity on the mean velocity scaling, near-wall turbulence statistics and turbulent structures are studied by performing DNS of a fully developed channel flow under the low-Mach-number approximation of the Navier–Stokes equations. Five variable-property cases ($CRe_\tau^\star$, $SRe_{\tau GL}^\star$, GL, LL, $SRe_{\tau LL}^\star$) with different relations for density and viscosity as a function of temperature are investigated. The different density and viscosity profiles are parametrised by means of the semilocal Reynolds number $Re_\tau^\star \equiv Re_\tau\sqrt{(\overline{\rho}/\overline{\rho}_w)}/(\overline{\mu}/\overline{\mu}_w)$, which is known from Patel *et al.* (2015) to be the governing parameter for turbulence statistics. The case $CRe_\tau^\star$ corresponds to a constant

wall-normal $Re_\tau^\star$ profile; for cases $SRe_{\tau GL}^\star$ and GL, the $Re_\tau^\star$ profile decreases towards the channel centre ($\mathrm{d}Re_\tau^\star/\mathrm{d}y < 0$), and for cases LL and $SRe_{\tau LL}^\star$, $Re_\tau^\star$ increases towards the channel centre ($\mathrm{d}Re_\tau^\star/\mathrm{d}y > 0$). Three constant-property cases (CP395, CP150, CP550) at different Re_τ values are also investigated to distinguish any Reynolds number effects from effects caused by property gradients.

Strong near-wall gradients in $Re_\tau^\star$ result in a failure to collapse the van Driest transformed mean velocity $\overline{u}^{vD}$ as a function of y^+. An extension of the van Driest transformation that accounts for the gradients in $Re_\tau^\star$ ($\mathrm{d}\overline{u}^\star = (1 + (y/Re_\tau^\star)\mathrm{d}Re_\tau^\star/\mathrm{d}y)\,\mathrm{d}\overline{u}^{vD}$) is derived based on the compelling collapse of the viscous stresses $(h/Re_\tau^\star)\,\mathrm{d}\overline{u}^{vD}/\mathrm{d}y$ for all cases when plotted as a function of the semilocal wall coordinate $y^\star$. A successful collapse of $\overline{u}^\star$ when plotted as a function of $y^\star$ was obtained for all of the investigated cases. The applicability of the transformation was also tested on adiabatic supersonic boundary layers of Bernardini & Pirozzoli (2011) and Pirozzoli & Bernardini (2011), which are known to show an excellent agreement of $\overline{u}^{vD}$ as a function of y^+. The new transformed velocity collapses supersonic cases at different Mach numbers. However, the supersonic cases showed a small increase in the log-law additive constant when compared with an incompressible turbulent boundary layer. In a recent work, Trettel & Larsson (2016) derived a similar transformation in terms of density and viscosity gradients, and applied it successfully to supersonic channel flows with isothermal cooled walls.

Near-wall gradients in $Re_\tau^\star$ also result in turbulence modification when compared with constant-property cases with similar Re_τ values. Partial success in accounting for this change in turbulence is obtained using the semilocal scaling, which accommodates the changes in viscous scales using local fluid properties. The success of the semilocal scaling is evident for the profiles of Reynolds shear stress and viscous shear stress. However, statistics like the r.m.s. of vorticity fluctuations, which are sensitive to the strong non-local interactions of the buffer layer vortical structures with the viscous sublayer, show a poor collapse in the near-wall region using the semilocal scaling. These strong non-local interactions are evident from the semilocally scaled streak spacing which tends to become universal after $y^\star \approx 12$–13, while it deviates significantly in the viscous sublayer for cases with $\mathrm{d}Re_\tau^\star/\mathrm{d}y \neq 0$. Furthermore, the failure of the semilocal scaling also occurs due to structural changes in turbulence that affect lifting and tilting of quasistreamwise vortices. These changes influence the Reynolds stress generation mechanism and the inter-component energy transfer for turbulent stresses. The influence of this failure on the scaling of the $\overline{u}^\star$ profile is negligible, since similarly to the Reynolds shear stress the mixing length is modified in the viscosity dominated region and therefore has a negligible influence on the transformed velocity profile.

The influence of $Re_\tau^\star$ gradients on vortical structures was studied using the three-dimensional swirling strength based on the instantaneous velocity gradient tensor. The orientation of these structures was determined using the real eigenvector of the tensor at the vortex centre. The analysis shows that, similarly to constant-property cases, the near-wall region in variable-property flows is also mostly populated by quasistreamwise vortices that are slightly inclined away from the wall and tilted towards the spanwise direction. Similarly to turbulence statistics, the near-wall turbulent structures are also strongly governed by the $Re_\tau^\star$ profile, and their dependence on individual density and viscosity profiles is negligible. Cases with $\mathrm{d}Re_\tau^\star/\mathrm{d}y > 0$ show an inflection point in $\overline{u}^{vD}$, causing a higher strain with respect to the wall. This increase in strain increases the mean forcing in the spanwise direction, which results in an increase in tilting of quasistreamwise vortices. The increased tilting

of the structures increases the asymmetry of the streaks, which are known to play an important role in maintaining the near-wall cycle and generation of strong shear layers (Johansson *et al.* 1991). This increased turbulence activity also causes an increased lifting of the structures and explains why cases with $\mathrm{d}Re_\tau^\star/\mathrm{d}y > 0$ show an increased momentum transfer in spite of lower turbulent kinetic energy. The increase in tilting of the structures also provides a physical interpretation for the increase in negative pressure–strain, which enables transfer of streamwise fluctuation energy towards spanwise and wall-normal components (Jeong *et al.* 1997). The opposite is true for cases with $\mathrm{d}Re_\tau^\star/\mathrm{d}y < 0$.

Acknowledgements

The authors would like to acknowledge access to large-scale computing facilities from the Netherlands Organisation for Scientific Research (NWO) through a grant with the dossier number SSH-223-13. The authors also wish to thank Dr S. Pirozzoli for providing additional information for his DNS data of supersonic turbulent boundary layers.

REFERENCES

ABE, H., KAWAMURA, H. & CHOI, H. 2004 Very large-scale structures and their effects on the wall shear-stress fluctuations in a turbulent channel flow up to $Re_\tau = 640$. *Trans. ASME J. Fluids Engng* **126** (5), 835–843.

ANTONIA, R. & KIM, J. 1994 Low-Reynolds-number effects on near-wall turbulence. *J. Fluid Mech.* **276**, 61–80.

BERNARDINI, M. & PIROZZOLI, S. 2011 Wall pressure fluctuations beneath supersonic turbulent boundary layers. *Phys. Fluids* **23** (8), 085102.

BOERSMA, B. J. 2011 A 6th order staggered compact finite difference method for the incompressible Navier–Stokes and scalar transport equations. *J. Comput. Phys.* **230** (12), 4940–4954.

BUSHNELL, D. M. & MCGINLEY, C. B. 1989 Turbulence control in wall flows. *Annu. Rev. Fluid Mech.* **21** (1), 1–20.

CHEN, H., ADRIAN, R. J., ZHONG, Q. & WANG, X. 2014 Analytic solutions for three dimensional swirling strength in compressible and incompressible flows. *Phys. Fluids* **26** (8), 081701.

CHERNYSHENKO, S. & BAIG, M. 2005 The mechanism of streak formation in near-wall turbulence. *J. Fluid Mech.* **544** (1), 99–131.

COLEMAN, G. N., KIM, J. & MOSER, R. D. 1995 A numerical study of turbulent supersonic isothermal-wall channel flow. *J. Fluid Mech.* **305**, 159–183.

DUAN, L., BEEKMAN, I. & MARTIN, M. P. 2010 Direct numerical simulation of hypersonic turbulent boundary layers. Part 2. Effect of wall temperature. *J. Fluid Mech.* **655**, 419–445.

DUAN, L., BEEKMAN, I. & MARTIN, M. P. 2011 Direct numerical simulation of hypersonic turbulent boundary layers. Part 3. Effect of Mach number. *J. Fluid Mech.* **672**, 245–267.

ELSINGA, G., ADRIAN, R., VAN OUDHEUSDEN, B. & SCARANO, F. 2010 Three-dimensional vortex organization in a high-Reynolds-number supersonic turbulent boundary layer. *J. Fluid Mech.* **644**, 35–60.

EYINK, G. L. 2008 Turbulent flow in pipes and channels as cross-stream inverse cascades of vorticity. *Phys. Fluids* **20** (12), 125101.

FOYSI, H., SARKAR, S. & FRIEDRICH, R. 2004 Compressibility effects and turbulence scalings in supersonic channel flow. *J. Fluid Mech.* **509**, 207–216.

GAD-EL HAK, M. 1990 Control of low-speed airfoil aerodynamics. *AIAA J.* **28** (9), 1537–1552.

GAO, Q., ORTIZ-DUENAS, C. & LONGMIRE, E. 2011 Analysis of vortex populations in turbulent wall-bounded flows. *J. Fluid Mech.* **678**, 87–123.

GUARINI, S. E., MOSER, R. D., SHARIFF, K. & WRAY, A. 2000 Direct numerical simulation of a supersonic turbulent boundary layer at Mach 2.5. *J. Fluid Mech.* **414**, 1–33.

HAMILTON, J. M., KIM, J. & WALEFFE, F. 1995 Regeneration mechanisms of near-wall turbulence structures. *J. Fluid Mech.* **287**, 317–348.

HUANG, P. & COLEMAN, G. N. 1994 Van Driest transformation and compressible wall-bounded flows. *AIAA J.* **32** (10), 2110–2113.

HUANG, P. G., COLEMAN, G. N. & BRADSHAW, P. 1995 Compressible turbulent channel flows: DNS results and modelling. *J. Fluid Mech.* **305**, 185–218.

JEONG, J., HUSSAIN, F., SCHOPPA, W. & KIM, J. 1997 Coherent structures near the wall in a turbulent channel flow. *J. Fluid Mech.* **332**, 185–214.

JIMÉNEZ, J., HOYAS, S., SIMENS, M. P. & MIZUNO, Y. 2010 Turbulent boundary layers and channels at moderate Reynolds numbers. *J. Fluid Mech.* **657**, 335–360.

JIMÉNEZ, J. & MOSER, R. D. 2007 What are we learning from simulating wall turbulence? *Phil. Trans. R. Soc. Lond.* A **365** (1852), 715–732.

JIMÉNEZ, J. & PINELLI, A. 1999 The autonomous cycle of near-wall turbulence. *J. Fluid Mech.* **389**, 335–359.

JOHANSSON, A. V., ALFREDSSON, P. H. & KIM, J. 1991 Evolution and dynamics of shear-layer structures in near-wall turbulence. *J. Fluid Mech.* **224**, 579–599.

KIM, J. & HUSSAIN, F. 1993 Propagation velocity of perturbations in turbulent channel flow. *Phys. Fluids* A*: Fluid Dynamics* **5** (3), 695–706.

KIM, J. & LIM, J. 2000 A linear process in wall-bounded turbulent shear flows. *Phys. Fluids* **12** (8), 1885–1888.

KLEWICKI, J., METZGER, M., KELNER, E. & THURLOW, E. 1995 Viscous sublayer flow visualizations at $R_\theta = 1\,500\,000$. *Phys. Fluids* **7** (4), 857–863.

KLINE, S., REYNOLDS, W., SCHRAUB, F. & RUNSTADLER, P. 1967 The structure of turbulent boundary layers. *J. Fluid Mech.* **30** (04), 741–773.

LAGHA, M., KIM, J., ELDREDGE, J. & ZHONG, X. 2011*a* A numerical study of compressible turbulent boundary layers. *Phys. Fluids* **23** (1), 015106.

LAGHA, M., KIM, J., ELDREDGE, J. D. & ZHONG, X. 2011*b* Near-wall dynamics of compressible boundary layers. *Phys. Fluids* **23** (6), 065109.

LECHNER, R., SESTERHENN, J. & FRIEDRICH, R. 2001 Turbulent supersonic channel flow. *J. Turbul.* **2**, 1–25.

LEE, J., YOON JUNG, S., JIN SUNG, H. & ZAKI, T. A. 2013 Effect of wall heating on turbulent boundary layers with temperature-dependent viscosity. *J. Fluid Mech.* **726**, 196–225.

LELE, S. K. 1992 Compact finite difference schemes with spectral-like resolution. *J. Comput. Phys.* **103** (1), 16–42.

LOZANO-DURÁN, A. & JIMÉNEZ, J. 2014 Effect of the computational domain on direct simulations of turbulent channels up to $Re_\tau = 4200$. *Phys. Fluids* **26** (1), 011702.

MAEDER, T. 2000 Numerical investigation of supersonic turbulent boundary layers. PhD Thesis, ETH Zürich, Institute of Fluid Dynamics.

MAEDER, T., ADAMS, N. A. & KLEISER, L. 2001 Direct simulation of turbulent supersonic boundary layers by an extended temporal approach. *J. Fluid Mech.* **429**, 187–216.

MAJDA, A. & SETHIAN, J. 1985 The derivation and numerical solution of the equations for zero Mach number combustion. *Combust. Sci. Technol.* **42** (3–4), 185–205.

MARQUILLIE, M., EHRENSTEIN, U. & LAVAL, J.-P. 2011 Instability of streaks in wall turbulence with adverse pressure gradient. *J. Fluid Mech.* **681**, 205–240.

MCMURTRY, P. A., JOU, W.-H., RILEY, J. & METCALFE, R. 1986 Direct numerical simulations of a reacting mixing layer with chemical heat release. *AIAA J.* **24** (6), 962–970.

MODESTI, D. & PIROZZOLI, S. 2016 Reynolds and Mach number effects in compressible turbulent channel flow. *Intl J. Heat Fluid Flow* **59**, 33–49.

MORINISHI, Y., TAMANO, S. & NAKABAYASHI, K. 2004 Direct numerical simulation of compressible turbulent channel flow between adiabatic and isothermal walls. *J. Fluid Mech.* **502**, 273–308.

MOSER, R. D., KIM, J. & MANSOUR, N. N. 1999 Direct numerical simulation of turbulent channel flow up to $Re = 590$. *Phys. Fluids* **11** (4), 943–945.

NEMATI, H., PATEL, A., BOERSMA, B. J. & PECNIK, R. 2015 Mean statistics of a heated turbulent pipe flow at supercritical pressure. *Intl J. Heat Mass Transfer* **83**, 741–752.

PATEL, A., PEETERS, J. W. R., BOERSMA, B. J. & PECNIK, R. 2015 Semi-local scaling and turbulence modulation in variable property turbulent channel flows. *Phys. Fluids* **27** (9), 095101.

PEI, J., CHEN, J., HUSSAIN, F. & SHE, Z. 2013 New scaling for compressible wall turbulence. *Sci. China Phys., Mech., Astron.* **56** (9), 1770–1781.

PIROZZOLI, S. & BERNARDINI, M. 2011 Turbulence in supersonic boundary layers at moderate Reynolds number. *J. Fluid Mech.* **688**, 120–168.

PIROZZOLI, S., BERNARDINI, M. & GRASSO, F. 2008 Characterization of coherent vortical structures in a supersonic turbulent boundary layer. *J. Fluid Mech.* **613**, 205–231.

PIROZZOLI, S., GRASSO, F. & GATSKI, T. 2004 Direct numerical simulation and analysis of a spatially evolving supersonic turbulent boundary layer at $M = 2.25$. *Phys. Fluids* **16** (3), 530–545.

RINGUETTE, M. J., WU, M. & MARTIN, M. 2008 Coherent structures in direct numerical simulation of turbulent boundary layers at Mach 3. *J. Fluid Mech.* **594**, 59–69.

ROBINSON, S. K. 1991 Coherent motions in the turbulent boundary layer. *Annu. Rev. Fluid Mech.* **23** (1), 601–639.

SCHOPPA, W. & HUSSAIN, F. 2002 Coherent structure generation in near-wall turbulence. *J. Fluid Mech.* **453**, 57–108.

SHADLOO, M., HADJADJ, A. & HUSSAIN, F. 2015 Statistical behavior of supersonic turbulent boundary layers with heat transfer at $M_\infty = 2$. *Intl J. Heat Fluid Flow* **53**, 113–134.

SMITH, C. & METZLER, S. 1983 The characteristics of low-speed streaks in the near-wall region of a turbulent boundary layer. *J. Fluid Mech.* **129**, 27–54.

SMITS, A. J. & DUSSAUGE, J.-P. 2006 *Turbulent Shear Layers in Supersonic Flow*. Springer.

SPINA, E. F. & SMITS, A. J. 1987 Organized structures in a compressible, turbulent boundary layer. *J. Fluid Mech.* **182**, 85–109.

TRETTEL, A. & LARSSON, J. 2016 Mean velocity scaling for compressible wall turbulence with heat transfer. *Phys. Fluids* **28** (2), 026102.

WU, Y. & CHRISTENSEN, K. T. 2006 Population trends of spanwise vortices in wall turbulence. *J. Fluid Mech.* **568**, 55–76.

ZHANG, Y.-S., BI, W.-T., HUSSAIN, F., LI, X.-L. & SHE, Z.-S. 2012 Mach-number-invariant mean-velocity profile of compressible turbulent boundary layers. *Phys. Rev. Lett.* **109** (5), 054502.

ZHOU, J., ADRIAN, R. J., BALACHANDAR, S. & KENDALL, T. 1999 Mechanisms for generating coherent packets of hairpin vortices in channel flow. *J. Fluid Mech.* **387**, 353–396.

ZONTA, F., MARCHIOLI, C. & SOLDATI, A. 2012 Modulation of turbulence in forced convection by temperature-dependent viscosity. *J. Fluid Mech.* **697**, 150–174.